Journal of Cardiovascular Magnetic Resonance®, 4(1), 63–84 (2002)

Poster Abstracts: Experimental MRI

202. Chronic Pulmonary Hypertension Changed Timing of Contraction But Not Pumping Capacity of the RV Hypertrophied Hearts—A Simultaneously Quantitative Analysis for LV and RV Hemodynamics with MRI

Yi-Jen Lin Wu,[1] Shinichi Kanno,[1] Chien Ho.[1] [1]*Pittsburgh NMR Center for Biomedical Research, Carnegie Mellon University, Pittsburgh, Pennsylvania, United States*

Introduction: Chronic pulmonary hypertension (PH) results in right ventricular (RV) hypertrophy (RVH), leading to RV dysfunction and heart failure. However, accurate quantitative analysis for RV function is challenging with conventional imaging modalities because of its complex shape. In addition, hemodynamic functions of RV have only been studied by invasive catheterization.

Purpose: Our goal of this study is to quantitatively evaluate RV and LV ventricular and hemodynamic functions non-invasively with MRI. Monocrotaline (MCT) induced chronic PH in rats, which in turn caused RVH. MCT-treated rats showed similar manifestations observed in the RV failing patients with severe PH. We also explored the role of angiotensin converting enzyme inhibitor (ACE-I) enalapril maleate as a potential therapeutic agent.

Methods: 1. Animal model: Male Sprague–Dawley rats were treated with monocrotaline (MCT). Three groups of rats were subjected to MRI evaluation: (1) MCT (40 mg/kg) only (2) MCT with ACE-I enalapril maleate (4.4 mg/kg/day) (3) Age and body-weight matched controls without treatment. 8 animals were studied for each group. MCT-treated rats received a single MCT injection 6 weeks prior to MRI examination. The MCT with ACE-I rats were treated with ACE-I daily for 4 weeks, starting 2 weeks after the MCT injection.

2. MRI protocols: Density-weighted spin-echo images were used to cover the 3D volume of the heart at 8 to 12 time points in a cardiac cycle. Myocardium mass were derived from ED wall volume and the specific gravity of myocardium (1.055 g/cm3). Cardiac tagging was achieved by modified DANTE sequence. All MRI scans were performed on Bruker AVANCE DRX 4.7-T system.

Results: 1. Morphology and myocardium mass: Severe RV hypertrophy (RVH) was developed 6 weeks after MCT injection (Fig. 1B). The RVH seemed to be reversed by ACE-I treatment (Fig. 1C). RV/LV + IVS wall mass ratios are 0.208, 0.729 and 0.235, for control, MCT only, and MCT + ACE-I treated rats respectively.

2. Timing of contraction: There is no significant change in blood pumping capacity upon MCT treatment. All 3 rat groups exhibited similar ejection fraction (EF) for both LV and RV. However, the timing for contraction is different. In control rats, both LV and RV reached end-systole (ES) at the similar timing. In contrast, MCT-treated rats showed delayed timing for ES. The systolic phase for LV of MCT rats prolonged about 25% (Fig. 2), which seemed to be corrected by ACE-I treatment. Moreover, some MCT-treated rats showed asynchronized cardiac phases for RV and LV. Figure 3 shows images acquired at different phases in a cardiac cycle of one MCT-treated rat. The end-diastole (ED) is defined as when the largest ventricular blood volume is present. The ED for LV (Fig. 3A) and RV (Fig. 3B) occurred at different times in a cardiac cycle. This phenomenon was found in about 1/3 of the MCT-treated rats but never in either control rats or MCT + ACE-I rats.

3. Contractility: MCT-treated rats showed worse contractility for LV wall but better in RV wall. Figure 4 shows wall thickening for LV free wall (LVFW), RV wall (RVW), and inter-ventricular septal wall (IVSW) for all three rat groups. MCT-treated rats exhibited decreased contractility for LVFW, probably due to geometric hindrance from the RVH. Interestingly, MCT-treated rats showed better contractility for

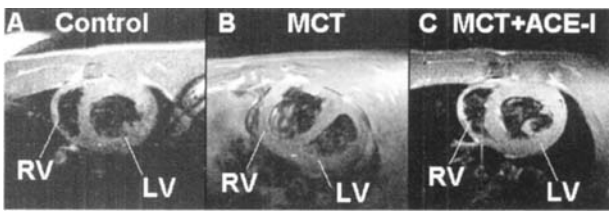

Figure 1. End-diastolic images for (A) control (B) MCT-treated, and (C) MCT + ACE-I treated rats.

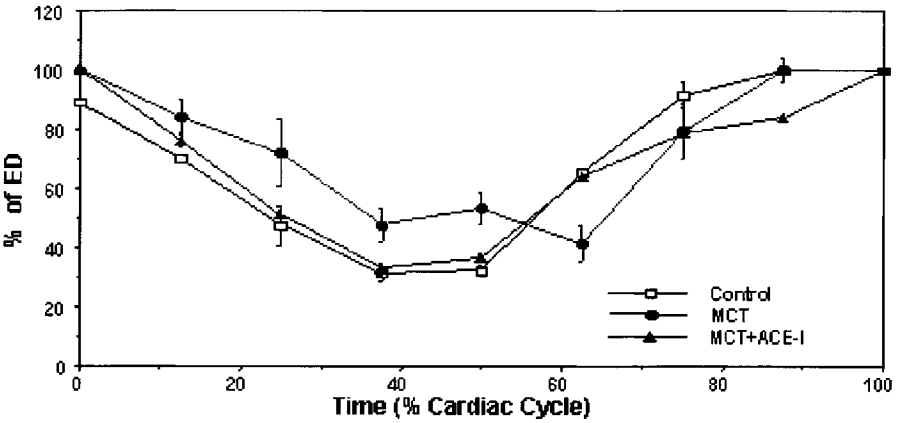

Figure 2. LV volume changes in time for all 3 rat groups. All values are normalized with ED. The data are presented as mean from all rats with standard deviation.

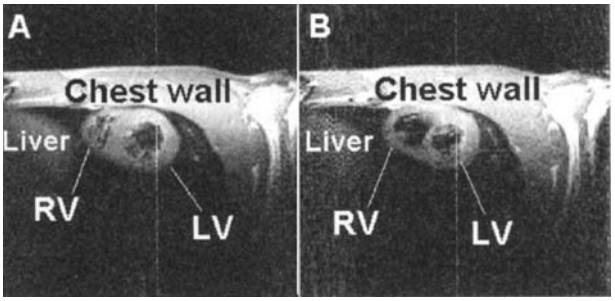

Figure 3. RVH caused by MCT-induced PAH resulted in asynchronized cardiac phases for RV and LV. The images are 50% out of phase in a cardiac cycle.

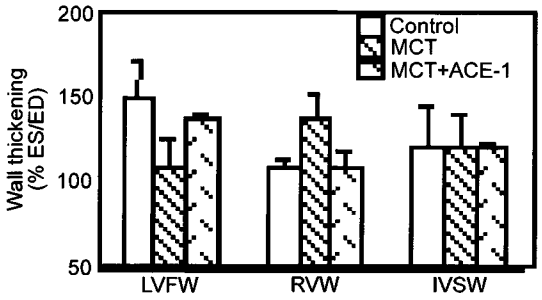

Figure 4. Contractility evaluated by wall thickening for LV free wall (LVFW), RV wall (RVW), and interventricular septal wall (IVSW) for all 3 rats groups. The data are presented as mean + std.

the RVW. The changes in LVFW and RVW are also reversed by ACE-I treatment. The changes in LV and RV contractility can be clearly seen with cardiac tagging (Fig. 5).

Conclusion: In addition to morphology, cardiac MRI is useful in analyzing RV dynamics. Our data showed that MCT-induced RVH did not change EF, rather the dynamics for contraction. MCT-treated rats exhibited hindered LV contractility associated with prolonged systolic phase. Some MCT-treated rats even showed asynchronized cardiac phases for LV and RV. Interestingly, RVH rats acquired better contractility for RV wall. All the MCT-induced changes can be reversed or attenuated by ACE-I treatment.

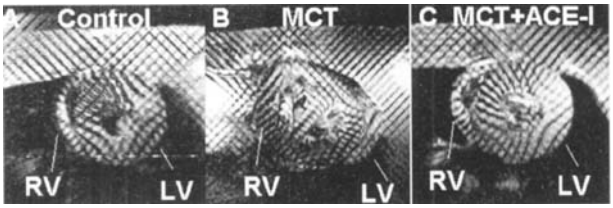

Figure 5. Contractility revealed by cardiac tagging.

203. Effects of MR Sequence and Contrast Agent Concentration on the Values of Fractional Distribution Volumes in Normal Canine Heart

Oliver Weber,[1] Charles Higgins,[1] Gabriele Krombach,[1] Maythem Saeed.[1] [1]*Department of Radiology, University of California at San Francisco, San Francisco, CA, USA*

Introduction: MRI offers different methods for assessment of myocardial viability including myocardial functional reserve, assessment of perfusion, or quantifying the area of late enhancement. Alternatively, it has been shown that determination of the partition coefficient λ or the closely related fractional distribution volume (fDV) allows outlining not only the infarcted region, but also the peri-infarction zone [1]. However, previous studies in rats, dogs, and humans have shown different λ values in normal myocardium; for example in rats, 0.33 ± 0.03 [2]; dogs, 0.40 ± 0.03 [3]; humans,

0.56 ± 0.03 [4]. In these studies different imaging sequences were used to determine λ.

Purpose: The purpose of the current study were 1) to test the optimum dose of extracellular MR contrast medium Gd–DTPA–BMA and 2) to examine different pulse sequences in evaluating the partition coefficient in normal myocardium.

Methods: Experimental protocol: Beagle dogs (n = 3) were enrolled in the current study. Anesthesia was initiated with 30 mg/kg sodium pentobarbital i.v. Additional injections were administered as required to maintain the heart rate between 70–80 beats/min. The animals were intubated and artificially ventilated with room air at a rate of 14 strokes/min. Heart rate and oxygen saturation were monitored continuously. A catheter placed in the left cephalic vein was used for administration of the contrast medium.

After baseline measurements, Gd–DTPA–BMA (Omniscan, Nycomed Amersham, UK) was administered as a bolus followed by constant contrast agent infusion (4% of the bolus per minute) to achieve equilibrium concentrations of 0.03 mmol/kg, 0.1 mmol/kg, and 0.3 mmol/kg. Equilibrium state distribution phase was assumed to be reached after 15 min of constant infusion. Fifteen minutes elapsed between each dose to ensure the washout of the contrast medium. A blood sample (3 ml) was obtained from each animal to determine the hematocrit. Changes in relaxation rate (ΔR1) following contrast agent administration were calculated as $1/T1_{postcontrast} - 1/T1_{precontrast}$.

Since the extracellular tracers used are in equilibrium distribution between tissue and blood after injection, the relative quantities in tissue over blood constitute partition coefficients λ. Assuming equal density of whole blood and myocardial tissue, fractional distribution volumes can be calculated as follows:

$$fDV = (\Delta R1_{myocardium}/\Delta R1_{blood}) \times (1 - hct),$$

where hct = hematocrit.

MRI: All experiments were performed on a Philips Gyroscan Intera I/T Cardiovascular system, equipped with Master Gradients (strength, 30 mT/m; slope, 150 mT/m/ms). Short axis image planes were defined on balanced fast-field echo (bFFE) images. T1 recovery image sets were achieved using a segmented turbo field echo (TFE) and a segmented gradient echo planar (EPI) version of a Look–Locker sequence [5]. After a non-selective 180° inversion pulse, 50 images were acquired with an interval of 30 ms between two consecutive images. Using an array of two elliptic surface coils (diameters, 17 cm and 14 cm), a matrix of 128 × 128 was acquired, covering a field of view of 20 cm with a slice thickness of 8 mm. Flip angle was 10°, and repetition time between two inversion pulses was three heartbeats. Further imaging parameters for the TFE sequence were: TR = 5.0 ms, TE = 3.0 ms, TFE factor = 6, minimum inversion delay 19 ms; and for EPI, TR = 30.0 ms, TE = 5.8 ms, EPI factor 5, minimum inversion delay 9 ms.

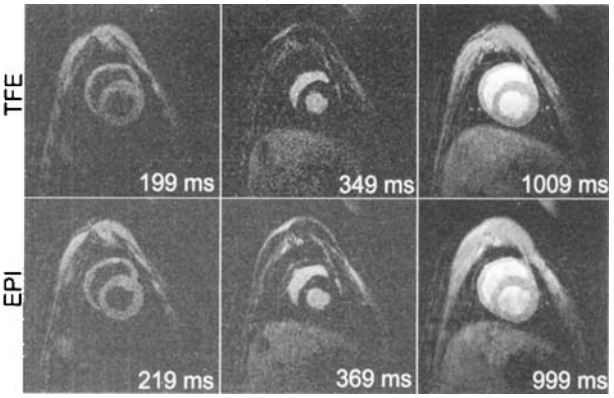

Figure 1. Look–Locker inversion recovery images, acquired with TFE and EPI at 0.1 mmol/kg contrast agent concentration, showing the time points of nulled blood, nulled myocardium, as well as approximately one second after inversion.

MR image sets, representing 50 different inversion times (examples are shown in Fig. 1), were processed using a tool developed at this institution. In 50 circumferential segments of mid-myocardium, mean signal intensities were calculated and an inversion recovery function was fitted to the time course to determine the T1 values of each individual segment.

Results: Table 1 shows the mean partition coefficients λ and fDV (mean ± standard error) for the two MR sequences used as well as for the three different contrast agent concentrations. The blood hematocrit was 44%, heart rate 73 ± 3 beats/min and oxygen saturation 97 ± 2%. There were no significant changes in heart rate or oxygen saturation following the administration of MR contrast media. At the clinically recommended dose (0.1 mmol/kg) both methods provided identical results, which are in line with the previously published data using analytical methods [6]. At higher Gd-concentration the mean values of λ were reduced, probably due to T2 and T2* effects of the high

Table 1

Partition Coefficients and Fractional Distribution Volumes (Mean ± Standard Error)

[Gd–DTPA–BMA] (mmol/kg)	λ (TFE)	fDV (TFE)	λ (EPI)	fDV (EPI)
0.03	0.39 ± 0.35	0.21 ± 0.19	0.33 ± 0.22	0.19 ± 0.12
0.1	0.31 ± 0.05	0.17 ± 0.02	0.32 ± 0.08	0.18 ± 0.04
0.3	0.24 ± 0.02	0.13 ± 0.01	0.27 ± 0.04	0.15 ± 0.02

Gd concentration. Furthermore, the TFE sequence showed greater dependence on Gd concentration, which may be a consequence of the shorter TR, causing a larger susceptibility to errors in the determination of T1. In the three examined dogs, there was no significant difference in fDV between anterior, lateral, posterior and septal walls of LV, suggesting equal density of whole blood and interstitial volume.

Conclusion: The TFE sequence produces optimum fDV values in normal myocardium at the clinically approved dose of 0.1 mmol/kg. Low and high doses overestimate and underestimate, respectively, fDV. The EPI sequence provides excellent values of fDV at low and medium doses, but not at the highest dose. At higher contrast agent concentrations, the results show lower spatial fluctuations. Measurements of fDV depend on both the dose and the pulse sequence. Further examinations will have to be performed to evaluate specificity and sensitivity of the methods with regard to classification of infarcted myocardium.

204. Detection of Minute Quantities of Fibrin on Human Unstable Atheromatous Plaques with Paramagnetic Nanoparticles at 1.5 T In Vitro

Patrick M. Winter,[1] Shelton D. Caruthers,[2] Ralph J. Fuhrhop,[2], Michael J. Scott,[1] Gregorio Sicard,[1] Patrick J. Gaffney,[3] Xin Yu,[1] Samuel A. Wickline,[1] Gregory M. Lanza.[1]
[1]*Cardiovascular MR Laboratories, Washington University in St. Louis, 660 S. Euclid Ave., Box 8086, Saint Louis, MO, United States;* [2]*Philips Medical Systems, Best, Eindhoven, Netherlands;* [3]*St. Thomas's Hospital, London, England, UK*

Introduction: Progressive microfissuring and thrombosis of the intimal surface of vulnerable atherosclerotic plaques are the precursors to stroke and myocardial infarction. Conventional imaging methods can identify lumenal stenosis, allowing the most severe narrowings to be treated surgically. The majority of thromboembolitic events, however, occur in vessels with only moderate stenosis. A non-invasive imaging method that distinguishes vulnerable plaques from stable lesions within these moderately narrowed vessels, therefore, would allow pinpoint treatment of the regions that are at risk for rupture.

In comparison to conventional MRI contrast agents, our site-targeted agent is designed to detect the specific biochemical markers of vulnerable plaques (i.e., fibrin deposition). By targeting these markers, not only can diseased and normal tissue be distinguished, but earlier detection of disease may be possible. Our targeted contrast system consists of a lipid-encapsulated, liquid perfluorocarbon nanoparticle (1). For in vitro experiments, this system utilizes avidin–biotin binding to couple specific monoclonal antibodies to the paramagnetic particle, but the nanoparticle can be directly coupled to the antibodies for in vivo applications (2). This research demonstrates the feasibility of fibrin-targeted paramagnetic nanoparticles for identification of microthrombosis in fractured atherosclerotic plaques in carotid artery segments from symptomatic patients.

Purpose: To demonstrate sensitive identification of unstable plaques in human carotid artery segments with T1-weighted signal enhancement after treatment with fibrin-targeted paramagnetic nanoparticles.

Methods: The fibrin-targeted paramagnetic nanoparticle contrast agent was produced by incorporating biotinylated phospolipid and a paramagnetic ligand (Gd–DTPA–BOA) into the outer lipid membrane of a perflurocarbon nanoparticle, as described previously (1). Segments of human carotid arteries were harvested from symptomatic patients during endarterectomy surgery. Arteries were suspended with 5-O sutures in 17 by 100 mm plastic snap-cap tubes. They were serially incubated with 150 μg biotinylated anti-fibrin antibodies (1H10) overnight at 4°C, 50 μg avidin for 1 hour at 37°C and 250 μl of the biotinylated paramagnetic nanoparticles for 1 hour at 37°C. Arteries were rinsed three times after each incubation step to remove unbound reactants.

MRI was performed on arteries with a clinical 1.5 T magnet (Gyroscan NT, Powertrak 6000, Philips Medical Systems, Best, Netherlands) using an 11 cm circular surface coil. Before and after treatment with the paramagnetic nanoparticles, T1-weighted and proton density images were collected with TR/TE of 300/24 ms and 3000/12 ms, respectively. The image resolution was 117 by 117 μm in-plane for T1-weighted images and 296 by 296 μm for proton density images with a 0.5 mm slice thickness. A horizontal line was drawn through the center of each artery and the signal intensity profile was calculated before and after treatment. The signal intensity was normalized relative to the signal from fiduciary markers with known, constant signal properties placed within the field of view. The change in signal intensity was calculated by subtracting the profile before treatment from the profile after treatment.

Results: The T1-weighted and proton density images collected before nanoparticle treatment showed areas of calcification (low signal amplitude) and lipid deposition (high T1-weighted signal amplitude) within the vessel walls. After treatment, the signal from the vessel walls was enhanced on T1-weighted images by 62 ± 7% (Fig. 1). The signal intensity of both the outer and inner walls increased dramatically after treatment (denoted AW in Fig. 2). Enhancement of the inner wall indicates the presence of fibrin deposits on the surface of vulnerable plaques. Since the samples are the result of endarterectomy surgery, the outer wall is actually comprised of plaque components, which contain high levels of fibrin. Therefore, enhancement of the outer wall is also anticipated. As expected, the proton density images did not show any significant changes in signal intensity after treatment.

Conclusion: These experiments suggest that fibrin-targeted paramagnetic nanoparticles can identify thrombus deposits in

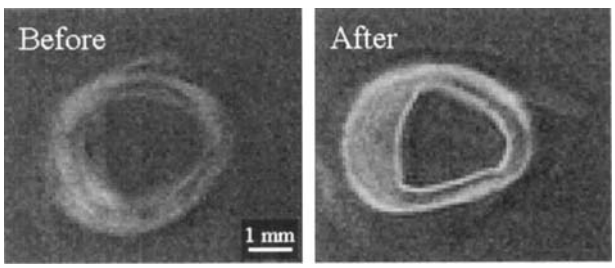

Figure 1. T1-weighted images of excised human carotid artery before and after treatment with fibrin-targeted paramagnetic nanoparticles.

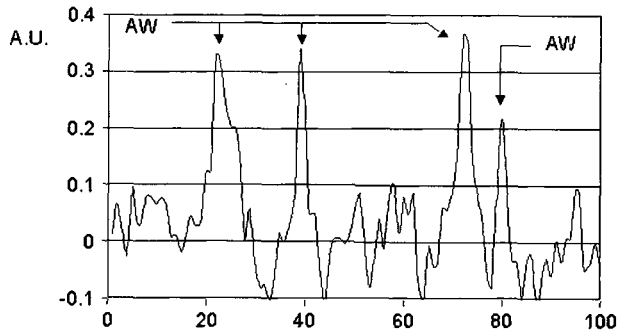

Figure 2. Change in T1-weighted signal intensity (in Arbitrary Units), showing increased signal intensity in arterial wall (denoted AW) after nanoparticle treatment.

symptomatic, ruptured atherosclerotic plaques in vitro. The enormous paramagnetic payload of our nanoparticle (approximately 88,000 Gd^{3+} ions per particle) provides significant signal enhancement despite the partial volume effects inherent in site-targeted contrast agents. We can detect the effects of a layer of particles 287 nm in diameter in an imaging voxel measuring 117 by 117 μm and 0.5 mm thick. These experiments utilized high resolution MRI in order to separate the signals from various plaque components, the arterial wall and the bound nanoparticles. But even with typical clinical resolutions (~1 mm in-plane), the nanoparticles create enough signal enhancement to detect thrombus formation (2).

This novel, targeted MRI agent may allow sensitive early detection and characterization of unrecognized vascular pathology in high-risk patients. In addition, the identification of vulnerable atherosclerotic plaques in vessels with moderate stenosis could lead to focused interventional therapy and reduction of morbidity and mortality of thromoembolism.

205. Strategies for Optimizing the Relaxivity of Fibrin-Targeted Paramagnetic Nanoparticles for Molecular Imaging by MRI

Patrick M. Winter,[1] Shelton D. Caruthers,[2] Ralph J. Fuhrhop,[1] Michael J. Scott,[1] Patrick J. Gaffney,[3] Samuel A. Wickline,[1] Gregory M. Lanza.[1] *[1]Cardiovascular MR Laboratories, Washington University in St. Louis, 660 S. Euclid Ave., Box 8086, Saint Louis, MO, United States; [2]Philips Medical Systems, Best, Eindhoven, Netherlands; [3]St. Thomas's Hospital, London, England, UK*

Introduction: Molecular imaging shows promise for the sensitive and specific detection of cardiovascular diseases. The high resolution, high contrast and non-invasive nature of MRI make it ideal for molecular imaging applications. Development of site-targeted MRI contrast agents, however, has been hampered due to the partial volume effects that obscure image enhancement at even the highest image resolutions. We have developed a novel site-targeted paramagnetic contrast agent consisting of a lipid-encapsulated perfluorocarbon nanoparticle incorporating tens of thousands of Gd–DTPA complexes on its lipid surface. Recently, we have reported dramatic changes in the relaxivity of these agents in solution upon alteration of the Gd–DTPA ligand (1). To further enhance the utility of these agents, we measured the relaxation of two formulations when bound to fibrin-rich human plasma clots.

Purpose: To determine the effects of two selected paramagnetic chelates on nanoparticle relaxivty when bound to a surface.

Methods: The site-targeted contrast agents were produced by incorporating biotinylated phospolipid into the outer lipid membrane of a perflurocarbon nanoparticle (2). One of two paramagnetic ligands (Gd–DTPA–BOA or Gd–DTPA–PE) was also incorporated into the lipid surface. Fresh frozen human plasma was used to form cylindrical clots, which were suspended in normal saline. Clots were serially incubated with 150 μg biotinylated anti-fibrin antibodies (1H10) overnight at 4°C, 50 μg avidin for 1 hour at 37°C and 250 μl of one of the biotinylated paramagnetic nanoparticle formulations (n = 3 for each formulation) for 1 hour at 37°C. Clots were rinsed three times after each incubation step to remove unbound reactants.

A clinical 1.5 T magnet (Gyroscan NT, Powertrak 6000, Philips Medical Systems, Best, Netherlands) was used with an 11 cm diameter circular surface coil. Inversion recovery images (TR/TE = 5000/26 ms, IR = 50 to 4500 ms) were collected with 61.5 by 61.5 μm in-plane resolution and 1 mm slice thickness. The images were fit pixel-by-pixel and R_1 values from three regions of interest (clot surface, clot interior and normal saline surrounding the clot) were calculated. The change in R_1 (ΔR_1) was calculated by subtracting R_1 at the clot interior from R_1 at the clot surface.

The surface area of each clot was determined from a 3-D T_1-weighted MRI scan (TR/TE = 802/23 ms, 123 by 123 μm resolution, 0.5 mm slice thickness). The clots were ashed in a muffle oven. The amount of Gd^{3+} bound to each clot was quantified by reconstituting the ashed samples and measuring T_1 in a Minispec NMR analyzer (Bruker, Inc., Milton, ON, Canada).

Results: The surface of clots treated with Gd–DTPA–PE nanoparticles showed about 30% greater image enhancement on T_1-weighted images compared to clots treated with Gd–DTPA–BOA nanoparticles (Fig. 1). Note the outer rim enhancement associated with binding one layer of nanoparticles onto the clot surface. The surface of BOA and PE clots had significantly different R_1 values ($p < 0.05$) of $1.26 \pm 0.05\,s^{-1}$ and $1.68 \pm 0.06\,s^{-1}$, respectively (Fig. 2). This corresponds to

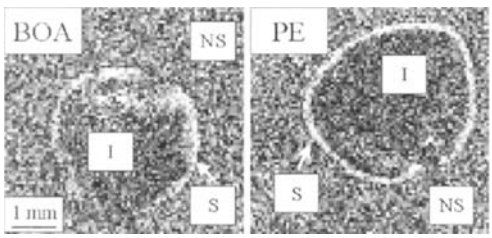

Figure 1. High resolution T_1-weighted image (IR = 1000 ms) of human plasma clots treated with fibrin-targeted Gd–DTPA–BOA or Gd–DTPA–PE nanoparticles. Abbreviations: S — clot surface, I — clot interior, NS — normal saline.

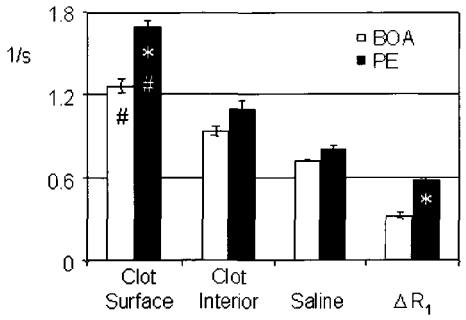

Figure 2. R_1 relaxation of clots treated with Gd–DPTA–BOA or Gd–DTPA–PE nanoparticles. Significant differences between *Gd–DTPA–BOA and Gd–DTPA–PE treated clots; #clot surface and both clot interior and saline ($p < 0.05$).

a 33% increase in relaxation as a result of incorporation of Gd–DTPA–PE into the nanoparticle lipid membrane. The R_1 values of the clot interior and saline were not significantly different between clots treated with Gd–DPTA–BOA and Gd–DTPA–PE ($p > 0.05$). The value of ΔR_1 was also significantly higher for clots treated with Gd–DTPA–PE (BOA: $0.33 \pm 0.02\,s^{-1}$, PE: $0.58 \pm 0.01\,s^{-1}$, $p < 0.05$). By subtracting out the contribution from the clot itself, the PE treated clots showed 76% higher relaxation rates than BOA treated clots.

The binding of nanoparticles to the clot surface was quantified to determine if differences in binding efficiency could account for the differences in relaxation. On average, $0.22 \pm 0.01\,\mu mol\ Gd^{3+}$ bound to the surface of BOA treated clots which had a surface area of $175 \pm 17\,mm^2$. PE treated clots had $0.22 \pm 0.02\,\mu mol\ Gd^{3+}$ bound to a surface area of $190 \pm 17\,mm^2$. None of these measurements show any significant differences ($p > 0.05$).

Conclusion: In summary, these experiments have shown that Gd–DTPA–PE nanoparticles have 33% higher R_1 relaxivity when bound to a surface compared to nanoparticles formulated with Gd–DTPA–BOA. Since the surface area and $[Gd^{3+}]$ of BOA and PE clots were identical, the differences in relaxation must be due to inherent differences in the paramagnetic influence of each formulation and not due to differences in particle binding efficiency. We have previously reported that the relaxivity of Gd–DTPA–PE nanoparticles suspended in water is more than three times greater than Gd–DTPA–BOA nanoparticles at 1.5 T (1). We believe the increased Gd–DTPA–PE relaxivity is due to greater water interaction because the Gd–DTPA–BOA complex is placed directly in contact with the lipid surface, whereas the Gd–DTPA–PE complex is suspended off the membrane through longer chemical linkages, permitting greater accessibility to protons in the local milieu. Some possible reasons why a 300% increase in intrinsic relaxivity observed in solution is reduced to a 33% increase when the nanoparticles are bound to a surface include partial volume effects and the dense packing of nanoparticles. The tight packing may reduce the interaction of water with the nanoparticles. Alternatively, such a high density of nanoparticles may cause the maximum relaxation effects to be approached even with the Gd–DTPA–BOA formulation. With a more sparse population of nanoparticles (i.e., targeting cell surface receptors) greater differences between the Gd–DTPA–BOA and Gd–DTPA–PE formulations may become apparent.

206. Characterization of Changes in Myofiber Structure at Cellular Level in Post-infarct Rat Heart Using Diffusion Tensor MRI

Junjie Chen,[1] Sheng-Kwei Song,[2] Wei Liu,[1] Mark Mclean,[1] Stacy Allen,[1] Samuel Wickline,[1] Xin Yu.[1] [1]*Cardiovascular MR Laboratories, Washington University, St. Louis, MO, USA;* [2]*Department of Chemistry and Radiology, Washington University, St. Louis, MO, USA*

Introduction: The myofiber organization of the heart is a key determinant of its mechanical properties. After myocardial infarction, the left ventricule undergoes structural changes including myofiber disarray and collagen deposition [1]. Recent studies of normal myocardium with diffusion tensor MRI (DTMRI) suggest that DTMRI may provide a fast and nondestructive technique to characterize myofiber architecture [2]. However, whether this technique is sensitive to changes associated with diseased state is largely unknown.

Purpose: The purpose of this study is to characterize myofiber structure in post-infarct rat heart with DTMRI to test the hypothesis that DTMRI can be used to delineate subtle structural changes that occur after myocardial infarction.

Methods: **Subjects:** Myocardial infarction was created in Fischer 344 rats by permanent ligation of the left coronary artery descending branch (LAD). The infarcted heart was excised and fixed with 10% formalin 4 weeks after infarction ($n = 3$). The control group comprised of sham-operated hearts prepared in the same way ($n = 3$). Upon imaging, one heart in each group was imaged in PBS solution. The rest were imaged in formalin.

Diffusion Tensor Imaging: DTMRI of fixed heart was performed on a Varian 4.7 T scanner using a solenoid RF coil. A multi-slice spin-echo sequence with diffusion sensitizing bipolar gradient was used. A total of 13 short-axis slices covering the whole left ventricle were acquired with the following parameters: TR, 4 sec; TE, 45 msec; slice thickness, 1 mm; field-of-view (FOV), $2 \times 2\,cm^2$; image matrix size, 128×128. These parameters yielded an in-plane resolution of $156 \times 156\,\mu m^2$. Diffusion gradients were applied along 6 non-

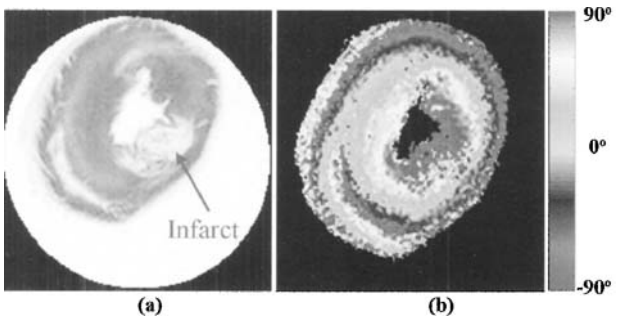

Figure 1. Trace map (a) and helix angle map (b) of a short-axis slice from a post-infarct rat heart.

Table 1

Trace of Diffusion Tensor and Relative Anisotropy in Selected ROI.

	Trace (mm^2/s)	RA
Infarct 1 (Formalin)	0.60 ± 0.05	0.13 ± 0.04
Infarct 2 (Formalin)	0.65 ± 0.06	0.11 ± 0.04
Infarct 3 (PBS)	0.93 ± 0.08	0.12 ± 0.05
Control 1 (Formalin)	0.44 ± 0.03	0.28 ± 0.04
Control 2 (Formalin)	0.40 ± 0.05	0.33 ± 0.04
Control 3 (PBS)	0.59 ± 0.06	0.26 ± 0.07

colinear directions with two *b*-values of 48 and 763 s/mm^2. Data acquisition time was 5 hours for 4 averages.

Imaging Processing: The diffusion tensor at each pixel was calculated from the 12 diffusion-weighted images. The three eigenvalues and their corresponding eigenvectors were then calculated. The trace map, ie. the sum of the three eigenvalues, and the relative anisotropy (RA) map were subsequently generated. Myofiber orientation, delineated by the primary eigenvector, was converted to helix angle representation (Figure 1b). Statistical analysis of myofiber helix angle at various transmural depth was performed.

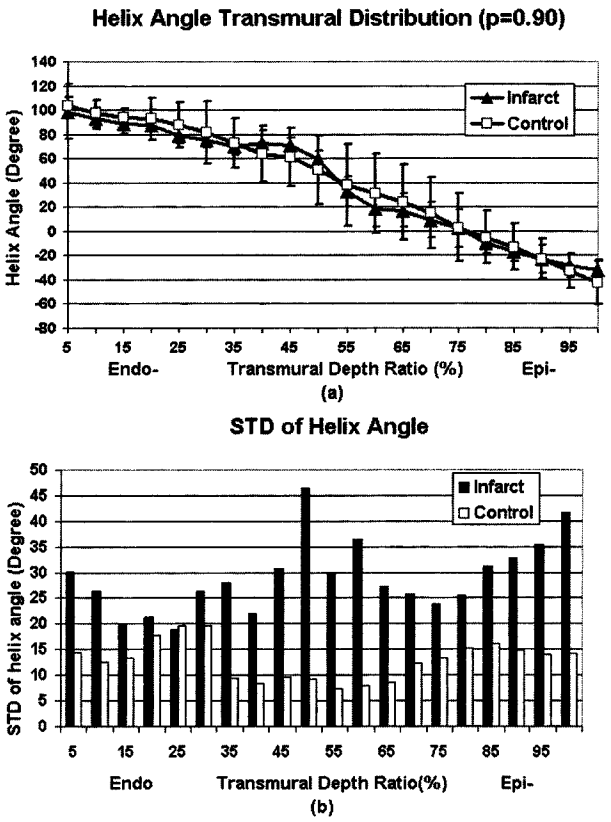

Figure 2. (a) Transmural course of the helix angle in both infarct and control groups; (b) Regional standard deviation of the helix angle at various transmural depth.

Results: All three eigenvalues of the diffusion tensor increased in infarct area, indicating increased magnitude of water diffusion. As a result, the infarct region appeared bright in the trace map (Figure 1a). Average trace value in infarct region increased by about 50% as compared to that of the control at the same location (Table 1). In addition to increased water diffusion, RA values decreased by 60–70% in infarct region. These changes are likely associated with tissue remodeling processes that occur at the cellular level.

Shown in Figure 2a are transmural variations of the helix angle in both infarct region and normal myocardium at the same location. Normal myocardium demonstrated continuous transition of the helix angle from +90° at endocardium to −40° at epicardium. Average helix angle in infarct area deviated only slightly from that of control hearts transmurally. However, much greater standard deviation of the helix angle was observed at the same transmural depth (Figure 2b), suggesting that while infarcted myocardium had preserved its normal global fiber struture, myofiber disarray might have occured at the microscopic level as an effect of local tissue remodeling and infarct expansion.

Conclusion: Global myofiber organization was unaltered in rats 4 weeks after infarction. However, infarct myocardium exhibited increased water diffusion and decreased diffusion anisotropy. Several cellular events may account for this increase in diffusion magnitude and decrease in diffusion anisotropy: 1. cell death leading to increased extracellular space; 2. local myofiber disarray due to collagen deposition; 3. angiogenesis characterized by leaky and randomly orientated vessels. This study demonstrated that DTMRI has the potential to provide a sensitive technique to detect subtle changes in myocardial structure that occur at cellular level.

207. Age Associated Regional Heterogeneity in Ventricle Twist and Shortening in Rats Quantified with MR Tagging

Wei Liu,[1] Junjie Chen,[1] Stacy Allen,[1] Mark Mclean,[1] Samuel Wickline,[1] Xin Yu.[1] [1]*Cardiovascular MR Laboratories, Washington University in St. Louis, Box 8086, 660 S. Euclid Ave., St. Louis, MO, USA*

Introduction: Ejection of blood from left ventricle is the result of several mechanisms including twist and shortening. Myocardial MR tagging provides a non-invasive, comprehensive method to assess the intrinsic myocardial deformation. It was evident from these studies that the myocardial twist and shortening are complex and closely related to the variations in transmural fiber orientation and local differences in ventricular morphology (1,3). While regional heterogeneity in twist and shortening has been recognized in both normal and diseased hearts, the relative contribution and regional non-uniformity of these different mechanisms are largely unknown.

Purpose: The purpose of this study is to characterize regional heterogeneity in left ventricular twist and radial shortening in Fischer 344 rats using MR tagging. Alterations in

ventricular twist and shortening associated with aging process were also evaluated.

Methods: Two age groups of normal Fischer 344 rats were studied: young (3 months, n = 4) and old (>20 months, n = 4). MR imaging was performed on a Varian 4.7 T scanner with a birdcage RF coil. The rats were sedated with 1% isofluorine by a nose cone. Tagged images of three short-axis slices were acquired. The midventricular slice was chosen at 50% of the distance between the atrioventricular valve plane and the apex. The basal and apical slices were chosen 3 mm above and below the midventricular slice repspectively. SPAMM1331 sequence was applied twice immediately after the ECG trigger, yielding a two-dimensional tag grid in the short-axis plane. The tagging sequence was followed by gradient-echo cine sequence with the following parameters: TR/TE,14.7 ms/3 ms; field-of-view, 6.5 cm × 6.5 cm; matrix size, 256 × 256; tagging resolution, 0.9 mm; slice thickness, 1.5 mm. A total of 15 frames were acquired during one cardiac cycle.

Images were analyzed with MATLAB based softwares developed in our laboratory. Epicardial and endocardial boders, intersecting tag points were traced interactively for all 15 frames. Subsequently, ventricular twist and radial shortening were computed relative to the center of ventricular cavity using 2D homogenous finite element analysis. Positive twist value indicated clockwise twist viewed from base. Positive radial shortening indicated inward motion. The left ventricle was segmented into anterior, lateral, inferior, and septum regions. Subendocardial and subepicardial twist and shortening in these four regions were thus calculated.

Results: Both young group and old group demonstrated similar patterns in net ventricular twist and shortening. As shown in Figure 1, anterior region showed clockwise twist at all three short-axis levels while septum always twisted counterclockwise from base to apex. Inferior and lateral regions reversed their twist from base to apex by twisting counterclockwise at base and twisting clockwise at apex. At base, anterior wall twisted clockwise while the other three regions twisted counterclockwise. At midventricle, lateral and anterior wall showed clockwise twist while septum and inferior wall exhibited counterclockwise twist. At apex, septum is the only region that twisted counterclockwise. All other regions twisted clockwise. Old rats manifested a trend of decreased net twist in all regions.

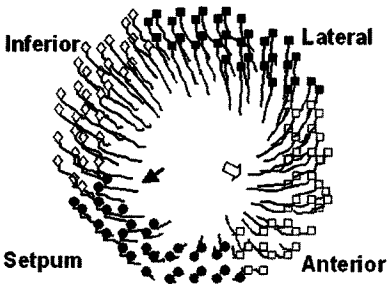

Figure 1. Left ventricle systolic motion trace. Black arrow indicates counterclockwise twist and write arrow indicates clockwise twist.

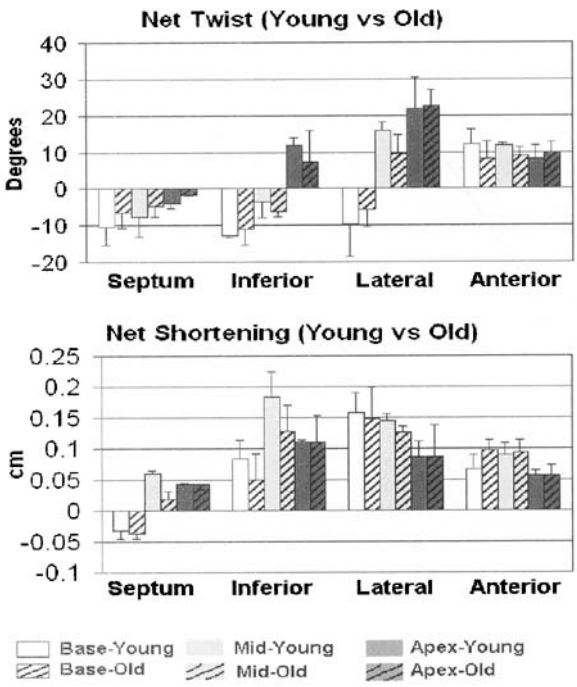

Figure 2. Subendocardial net ventricular twist (upper) and shortening (lower) from base to apex in yound and old rats.

Radial shortening was demonstrated in all four regions at midventricular and apical levels. At base, septum underwent radial lengthening. At midventricular level, net septum shortening was significantly smaller than that of other regions. Old rats manifested greater differences between subendocardial and subepicardial shortening. Of statistical significance, net lateral shortening was 0.126 ± 0.010 cm in subendocardial area and 0.095 ± 0.012 cm in subepicardial region ($p < 0.05$) at midventricle. At apex, net septal shortening was also significantly larger in subendocardial region than in subepicardial region (0.042 ± 0.002 cm vs 0.026 ± 0.002 cm, $p < 0.05$).

Conclusion: Although old rats demonstrated a trend of decreased net twist, both young and old rats showed similar patterns of regional heterogeneity in local twist and radial shortening among all anatomic segments at all levels. Subendocardial region manifested larger twist and shortening than subepicardial region. Anterior wall demonstrated consistent clockwise net twist. Septum demonstrated consistent counterclockwise twist and also has the smallest radial shortening. Although few data regarding myocardial strain in rats exist in current literature, our findings are consistent with other MRI tagging data from human subjects (1). This regional heterogeneity in twist likely reflects the heterogeneity of myofiber architecture (2). Anatomic studies have shown significant fiber crossover between LV and RV along the anterior interventricular sulcus. This feature might account for the greater clockwise twist values for the anterior wall. The consistent counterclockwise twist of septum and the least radial shortening might due to the interaction from right ventricle.

208. Magnitude of Misregistration Errors with Breath-Hold Cardiac MR

Cory Swingen,[1] Ravi Seethamraju,[1] Norbert Wilke,[1] Michael Jerosch-Herold.[1] [1]*University of Minnesota, 420 Delaware St. SE, Minneapolis, Minnesota, United States*

Introduction: Most MR methods used to image the cardiac anatomy, or coronary arteries, require repeated breath-holds to adequately cover the heart. Variations in the diaphragm position from one breath-hold to the next alter the position of the heart, resulting in slice misregistration errors.

These effects introduce errors and artifacts e.g. in the areas of MR angiography, 3D modeling and global calculations where the accuracy of the slice location and position of the left ventricle (LV) in the MR image are a fundamental assumption to the correct registration of data from multiple images, or data sets. There exist different options to correct or minimize these errors including centroid-fitting, during post-image processing, or navigator-gating during the exam.

Purpose: The objective of this study is to obtain quantitative information on the respiratory motion of the heart during normal breathing and determine the effects of multiple breath-holds on the accuracy of the position of the LV in the MR image. In particular we are interested in cardiac motion parallel and perpendicular to the long and short-axis routinely used as reference frames in clinical cardiac MR studies.

Methods: For the assesment of cardiac motion seven volunteers were imaged using a fast single-shot 2D TrueFISP sequence with ECG triggering and fat suppression to picture the LV in a horizontal long-axis (LA) and short-axis (SA) plane. Both slices were acquired within one R–R interval. To cover the tidal breathing range, subjects were asked to breath normally and 45 images were acquired covering the breathing cycle from normal inspiration to expiration. To evaluate the misregistration errors due to multiple breath-holds subjects were asked to exhale and hold their breath at end expiration during image acquisition. This procedure was repeated until 15 images were acquired, each representing a different end-expiration breath-hold.

To quantify the position of the LV and the diaphragm we measured the coordinates of particular anatomic landmarks in each image. In the long-axis images we measured the midpoint of the diaphragm (D), the apex (A), the anterior margin (AM) and posterior margin (PM) of the base of the left ventricle (B). From these points we determined a central long-axis and the base, defined as the midpoint of the segment connecting points

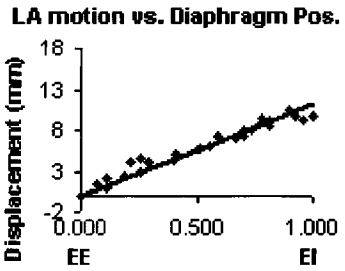

Figure 1. LA motion of the base.

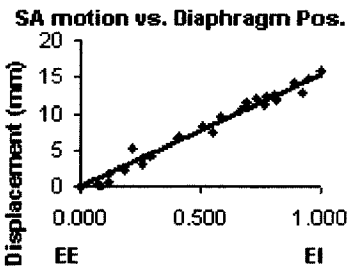

Figure 2. SA motion of the base.

AM and PM. In the SA images we calculated the center of the LV as the centroid of the segmented epicardial contour.

From previous studies we know that the superior–inferior (SI) motion of the heart is linearly related to the SI position of the diaphragm. From this information we were able to determine the most end-expiration image, calculate the displacement of each landmark and resolve its motion in the LA (Fig 1) and SA (Fig 2) direction from end-expiration (EE) to end-inspiration (EI).

A segmented gradient echo sequence was also used to image the entire LV (~10–12 SA slices) within a single breath-hold to assess the shape of the LV without breath-hold artifacts. We fit the x and y components of the endocardial centroids as a function of slice position to determine a corrective-fitting polynomial for minimizing SA slice misregistration.

Results: Our results indicate that the magnitude of the motion in the SA plane dominates over its through-plane (LA) motion at both the base and the apex. At the base the LA displacement of the LV was 11.07 ± 2.01 mm and in the SA direction 15.4 ± 3.13 mm. Motion of the apex in along the LA was 5.5 ± 2.95 mm and in the SA 15.5 ± 5.56 mm. Table 1 illustrates the amount of slice-to-slice misregistration for repeated end-expiration breath-holds. The LA misregistration is approximately equal from the base to the apex while the SA motion is more pronounced towards the apex.

From the single breath-hold images we found a simple 2nd order polynomial fit of the endocardial centroids minimized the SA slice misregistration.

Conclusion: The results we present in this study indicate the motion of the heart varies linearly with the diaphragmatic position. In addition we have shown that the variations in breath-holds produce non-negligable errors in the position of the LV which should be considered and corrected as necessary.

This work was supported by ROI HL65394-01 from NHLBI.

Table 1

Breath-Hold Misregistration (mm)

	Apex	Mid	Base
LA plane	3.09 ± 1.50	3.01 ± 1.68	3.00 ± 1.82
SA plane	3.98 ± 1.08	4.16 ± 1.62	3.80 ± 1.89

209. Nanoparticle Emulsions: Novel Uses as Combined MRI Contrast Agents and Targeted Drug Delivery Vehicles for Molecular Imaging and Therapy

Gregory Lanza,[1] Xin Yu,[1] Patrick Winter,[1] Dana Abendschein,[2] Kerry Karukstis,[3] Michael Scott,[1] Ralph Fuhrhop,[1] David Scherrer,[2] Samuel Wickline.[1]
[1]*Cardiovascular MR Laboratory, Washington University, St. Louis, MO, USA;* [2]*Washington University, Campus Box 8086, St. Louis, MO, USA;* [3]*Harvey Mudd College, 12th and Columbia, Claremont, CA, USA*

Introduction: Restenosis often complicates coronary angioplasty through the proliferation and migration of vascular smooth muscle cells from the media to the intima and the synthesis of extracellular matrix. A ligand-directed nanoparticle was developed that can penetrate into the tunica media through microfractures created by balloon-overstretch injury and can specifically attach to activated smooth muscle cells via membrane epitopes, such as up-regulated tissue factor (1). This unique nanoparticle formulation could provide prolonged release of therapeutic agents that can inhibit neointimal hyperplasia. Moreover, the paramagnetic properties of the nanoparticle permit the localization and quantification of drug delivery to be ascertained by MRI techniques.

Purpose: The objective was to demonstrate MR imaging and quantification of targeted drug delivery using tissue factor-targeted, paclitaxel nanoparticles.

Methods: The perfluorocarbon contrast agent incorporates biotinylated phosphatidylethanolamine into the outer lipid monolayer of a perfluorocarbon emulsion. The 2% lipid surfactant co-mixture included paclitaxel at concentrations of 0.0 mole%, 0.2 mole% or 2.0 mole% and gadolinium diethylene-triamine-pentaacetic acid-bis-oleate at concentrations of 0 mole% or 20 mole%. A polyclonal antibody to the extracellular domain of recombinant porcine tissue factor was employed to target vascular smooth muscle cells (VSMC) using avidin–biotin intermediate steps. In general, porcine aortic smooth muscle cells grown as previously reported, were incubated for 2 days, and then exposed to treatments (below) for 30 minutes. Unbound nanoparticles were washed from wells, and cultures were grown to ~85% confluence (i.e., about 3 days). Attached viable cell numbers were counted. VSMC (n=9/treatment) were treated with TF-targeted or non-targeted paclitaxel nanoparticles incorporating 0.0 mole%, 0.2 mole% or 2.0 mole% paclitaxel. A subset of cultures were filled with 2% agarose and stacked for MR imaging. Magnetic resonance imaging of the targeted and untargeted cells was performed at 4.7 T on a Varian INOVA system (Varian Associates, Palo Alto, CA). Spin-echo proton images were acquired using a 3 cm custom designed birdcage coil. Sagittal T1-weighted spin-echo images of the plating wells were acquired. Imaging parameters were: TR, 150 ms; TE, 30 ms; FOV, 4 × 4 cm; data matrix, 512 × 256; slice thickness, 1 mm, yielding an in-plane resolution of 156 × 156 μm. 19F signal was measured at 4.7 T by 19F MRI using a 1.5 cm single turn solenoid coil, dual-tuned to 1H and 19F. The imaging parameters were: TR/TE/a, 5 s/6.3 ms/90°; FOV 2 cm × 2 cm × 1 mm; image matrix 256 by 256. Paramagnetic nanoparticles containing 0 mole% or 20 mole% Gd–DTPA were diluted serially from 50% to 1% and the 19F signal intensity of each dilution was measured spectroscopically at 0.47 T on a Bruker MQ20 Minispec NMR Analyzer and quantified with respect to reagent grade perfluorooctylbromide.

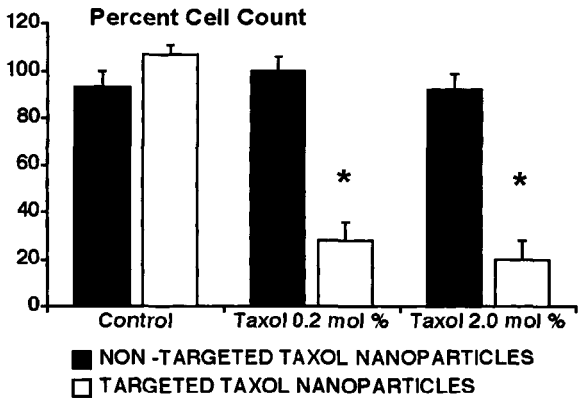

Figure 1. Paclitaxel nanoparticles reduce smooth muscle cell growth.

Results: Control nanoparticles, whether targeted or untargeted, exhibited no effect on smooth muscle cell proliferation. TF-targeted paclitaxel nanoparticles markedly decreased cell proliferation significantly ($p < 0.05$) at both dosages (74% and 81% decreases, respectively; $p < 0.05$; Figure 1). Non-targeted paclitaxel nanoparticles exhibited no effect on cell proliferation. These data suggest that the effectiveness of therapeutic nanoparticles is facilitated by the ability of the paclitaxel nanoparticles to bind and interact with the target cell surface.

Unlike other drug delivery systems, the nanoparticles provide a prominent T1-weighted MR signal when formulated with gadolinium. Magnetic resonance images obtained at 4.7 T clearly reveal that even a submicron layer of paramagnetic nanoparticles on a monolayer of cells in culture can be readily detected with T1-weighted spin-echo imaging despite a greater than 100-fold partial volume dilution effect (Figure 2). Image intensity was nearly two-fold greater from nanoparticle targeted

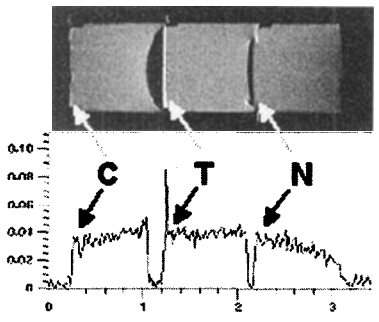

Figure 2. Smooth muscle cells imaged in wells (upper panel) bind targeted nanoparticles (arrows show contrast effect at the cell layer) and demonstrate enhanced T1-weighted signal amplitude (Lower panel) only for specifically targeted (T) nanoparticles.

cells (T; 0.062 ± 0.004) as compared with nontargeted cells (C or N; 0.032 ± 0.002).

In addition, the presence of the nanoparticles bound to the cell surface was verified by detection of the fluorine signal with MR spectroscopy. This unique feature of targeted perfluorocarbon nanoparticles allows high-resolution MRI detection of the nanoparticles at the target site to be confirmed by independent co-localization of the fluorine signal, potentially eliminating confusion with other tissue components or artifacts. Signal amplitude (0.47 T) was unaffected by the presence of gadolinium and was linearly related to perfluorocarbon fluorine concentration, and by direct inference to nanoparticle number.

Conclusion: Ligand-targeted paramagnetic nanoparticles are unique molecular imaging agents that may be useful for targeting and quantifying delivery of therapeutic agents to treat post-angioplasty restenosis and providing prognostic information for clinical management.

210. The Impact of Spatial Resolution and Respiratory Motion on Magnetic Resonance Plaque Characterization

Michael Schär,[1] W Yong Kim,[2] Matthias Stuber,[3] Peter Boesiger,[1] Warren J Manning,[3] René M Botnar.[3] [1]*University and ETH Zurich, Institute of Biomedical Engineering, Zurich, Switzerland;* [2]*Department of Cardiology, Brendstrupgaardsvej, Aarhus, Denmark;* [3]*Beth Israel Deaconess Medical Center, Cardiovascular Division, Boston, Massachusetts, United States*

Introduction: Studies have shown that magnetic resonance (MR) imaging has the potential for characterization of atherosclerotic plaque and the assessment of plaque burden [1–3]. As the physical dimension of the lipid core and the fibrous cap are usually sub-millimeter, spatial resolution and thus partial volume effects might heavily affect the accuracy of quantitative and qualitative measurements. For coronary artery plaque imaging, cardiac and respiratory motion are an additional challenge and are likely to decrease the accuracy of plaque burden measurements and the ability to characterize atherosclerotic plaque.

Purpose: We therefore sought to investigate the impact of spatial resolution and respiratory motion on the ability to differentiate between plaque components and to accurately assess vessel wall thickness.

Methods: Numerical simulations and phantom measurements of a vessel wall model were performed. Lumen diameter (3 mm) and wall thickness corresponded to the size of a "normal" wall (1 mm) and a "diseased" (2 mm & 3 mm) coronary artery wall. The wall consisted of three concentric tissue layers (fibrous cap, lipid core, and smooth muscle) with T1 and T2 values derived from in-vivo and in-vitro measurements [1,4]. The simulated and measured images were obtained with a T2 weighted double inversion fast spin echo (TSE) sequence with a TE of 40 ms, a TR of 2 cardiac cycles and linear profile order. In-plane spatial resolution varied from 167 to 1333 μm. Respiratory motion was simulated using a subject derived breathing curve. Navigator gating with a diaphragmatic (cardiac) acceptance window of 1.7 mm (1 mm) and 5 mm (3 mm) was performed and a scaling factor of 0.6 was applied [5].

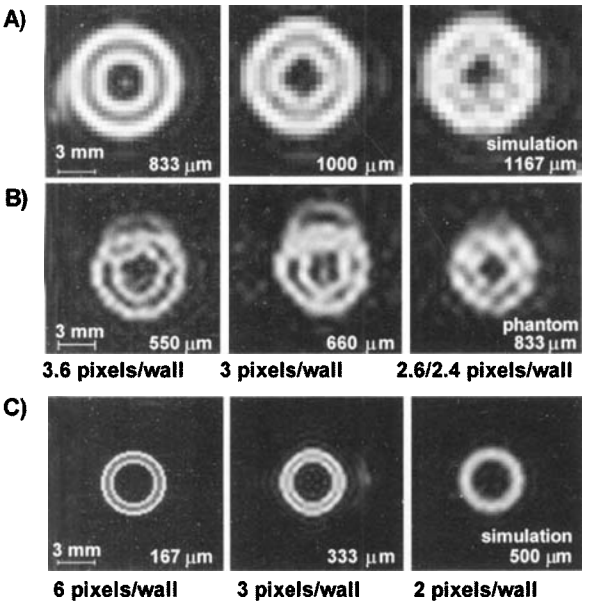

Figure 1.

Results: Visual tissue characterization required an in-plane spatial resolution of ≥3 pixels per wall thickness (≥1 pixel per tissue layer) (Figure 1).

Fourier zoomed cross sections of simulated (A, C) and measured (B) vessels with different spatial resolutions for a TSE double inversion sequence. The first row shows simulated images of a "diseased" (A) vessel wall with the corresponding phantom images in the second row (B). The concentric tissue layers could be visually discriminated at a resolution of at least 3 pixels per wall thickness, which corresponds to 1 pixel per tissue layer. Analogous findings were made for the simulated normal (C) vessel wall.

With superimposed respiratory motion a gating window of ≤1 mm (≤ 1.7 mm on diaphragm) was necessary to allow for differentiation of the three tissue layers of the "normal" vessel wall (1 mm). For the "diseased" vessel wall (3 mm), the three tissue layers could be visualized properly even with a 3 mm (=5 mm on diaphragm) gating window (Figure 2).

Fourier zoomed simulated vessel wall images with superimposed respiratory motion. Visual discrimination of the tissue layers was possible at a spatial resolution of 3 pixels per wall

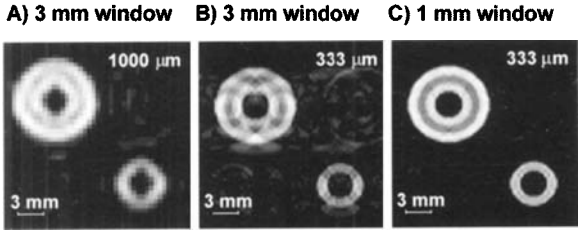

Figure 2.

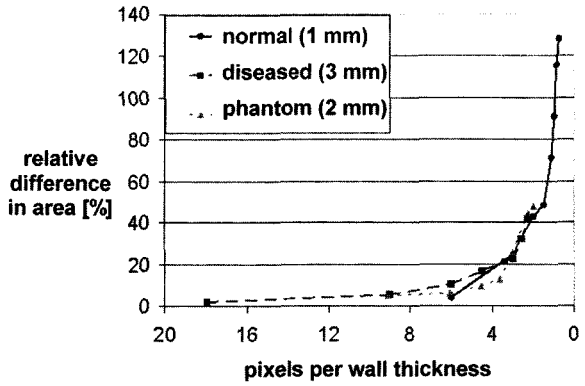

Figure 3.

thickness. For a "normal" vessel wall a 1 mm gating window was necessary (C), whereas for the "diseased" vessel wall a 3 mm gating window was sufficiant (A).

Due to partial volume effects, wall area was overestimated and lumen area was underestimated. The overestimation and the underestimation increased with lower spatial resolution. For spatial resolutions with ≤4 pixels per wall thickness/lumen diameter, the area quantification errors exceeded 20% and rapidly increased with lower resolutions. With higher spatial resolution the measurement error decreased asymptotically (Figure 3). Motion related wall and lumen area quantification errors did not show a strong correlation with spatial resolution.

The relative measurement error of the wall area depending on the spatial resolution. For an error of ≤20%, the spatial resoltion has to be ≥4 pixels per wall thickness.

Conclusion: Tissue characterization in a "normal" coronary vessel wall requires an in-plane resolution of approximately ≤330 μm with less stringent requirements for "diseased" vessels. Spatial resolution has a greater impact on the ability to discriminate tissue layers than respiratory motion.

211. MR Quantification of Extent of Microvascular Injury at 3 and 24 Hours Post-infarction Reperfusion Using Clariscan as a Blood Pool MR Contrast Medium

Gabriele A. Krombach,[1] Charles B. Higgins,[1] Maythem Saeed.[1]
[1]*Department of Radiology, University of California San Francisco, Parnassus Avenue 505, San Francisco, CA, USA*

Introduction: Microvascular injury plays a major role in the pathophysiological circuit of myocardial injury and healing. Scarabelli et al (1) have recently demonstrated that apoptosis of endothelial cells precedes cardiac myocyte cell apoptosis in the very early stage of reperfusion and peaks at 1 hour of reperfusion. Mediators released from apoptotic endothelial cells trigger apoptosis of cardiac myocytes (1). Several studies have indicated that the severity of myocardial damage is associated with the extent and degree of microvascular injury (2).

Extracellular MR contrast agents have been successfully used in patients for delineating transmural and non-transmural infarction (3) and in assessing myocardial viability (4). However, these agents rapidly distribute into the extravascular space, which eliminates their potential for probing of microvascular integrity. On the other hand, blood pool agents, represented by Clariscan, have recently been proposed for assessment of perfusion (5) and microvascular integrity (6).

Purpose: 1) to characterize microvascular injury at 3 and 24 hours after reperfusion using sequential MR imaging with the blood pool MR contrast medium Clariscan, and 2) to quantify and compare the extent of microvascular injury on contrast enhanced MR imaging with that measured on T2 weighted spin-echo MR images, area at risk and infarction at autopsy.

Methods: Fourteen rats were included into this study. After thoracotomy, ischemic microvascular injury was produced by placing a snare loop around the left anterior coronary artery. Two groups of rats were randomly assigned to either 3 h (n = 7), or 24 h of reperfusion (n = 7). MR images were obtained at a 2 T system (Omega CSI, Bruker Instruments, Fremont CA) using ECG-gating. All animals received 3 mg Fe/kg (0.05 mmol/kg) Clariscan.

T1-weighted spin-echo images were acquired before and serially for 45 min after injection of the contrast medium at a single slice location to assess the accumulation of the contrast medium in the injured region and to quantify the changes in the size of differentially enhanced areas. At 45 min, multislice images were acquired to cover the left ventricle. Acquisition parameters were: TR/TE 300/12 ms, matrix size = 256 × 128 data points interpolated to 256 × 256 during Fourier transformation, FOV 50 × 50 mm, slice thickness = 2 mm, 4 acquisitions, scan time = 2.5 min.

T2-weighted spin-echo images were acquired to define the hyperintense region presumed to represent edematous ischemically injured myocardium. Acquisition parameters for these images were: TR/TE = 2000/40 ms, matrix size = 256 × 256, FOV = 50 × 50 mm, slice thickness = 2 mm, 2 acquisitions, scan time = 8.5 min. After imaging, the left anterior coronary artery was reoccluded and phthalocyanine blue dye was injected intravenously to define the area at risk. Sliced LV was incubated in triphenyltetrazolium chloride (TTC) solution to define infarcted myocardium.

Results: Characterization of microvascular injury: T2-weighted spin-echo images showed the ischemically injured region as a bright zone at 3 and 24 hrs post-infarction. On T2-weighted spin-echo images the size of this bright zone was 45 ± 3% of LV at 3 hrs and 39 ± 2% at 24 hrs. The injured region was not visible on T1-weighted baseline images. Clariscan improved visualization of the region with microvascular damage in both groups of animals. Accumulation of Clariscan was best reflected by the signal intensity ratios of injured/normal myocardium (3 hrs at baseline 0.98 ± 0.01 and after 25 min post-injection 1.7 ± 0.08) and after (24 hrs at baseline 0.99 ± 0.01 and after 25 min post-injection 1.4 ± 0.09). At 3 hours, accumulation of Clariscan in the previously ischemic region suggests presence of microvascular injury. The slow accumulation of the contrast medium in the injured region at 24 hrs may be attributed to the presence of microvascular obstruction (Fig. 1) (7).

Quantification of the extent of microvascular injury: On Clariscan contrast enhanced MRI the size of differentially enhanced region was slightly but significantly smaller after 24 h

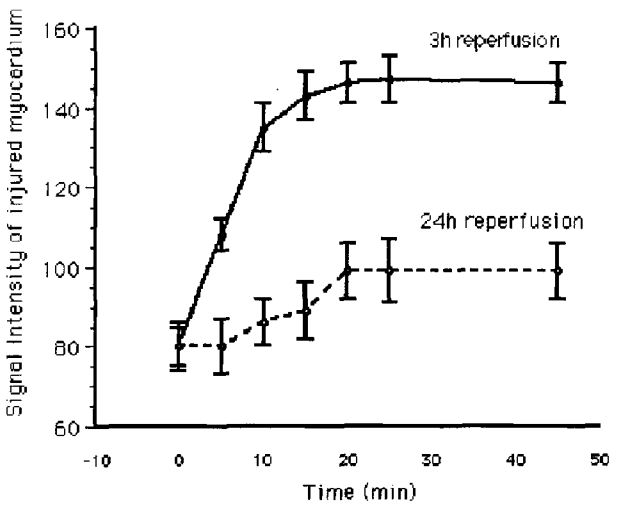

Figure 1. Accumulation of Clariscan in the injured region.

(39 ± 2% of LV) than that after 3 h of reperfusion (44 ± 2% of LV). Bland–Altman analysis revealed overestimation of Clariscan enhanced region of 15 ± 7% after 3 h and 10 ± 5% after 24 h of reperfusion. The decline in the size of the enhanced region (from 15 to 10%) may be attributed to the reduction of interstitial edema in the peri-infarcted region. Size of area at risk (50 ± 2%, versus 51 ± 2%) and true infarction (29 ± 2%, versus 29 ± 2%) were identical in both groups (P = NS).

Conclusion: MRI with the use of blood pool contrast media may have potential to noninvasively characterize and map the extent of microvascular injury in reperfused ischemically injured myocardium. The reduction in the extent of microvascular injury suggests reduction of interstitial edema and recovery of reversibly injured microvessels. Furthermore this finding supports the notion (1) that functional impairment of vascular endothelial cells may precede functional impairment of cardiac myocytes.

212. Partition Coefficient of Gd–DTPA in a Canine Model of Hibernating Myocardium

Katie S Lekx,[1] Frank S Prato,[1] Jane Sykes,[2] Gerald Wisenberg.[2]
[1]*University of Western Ontario, Dept. of Nuclear Medicine & MR, London, Ontario, Canada;* [2]*Lawson Health Research Institute, Department of Nuclear Medicine and MR, London, Ontario, Canada*

Introduction: Hibernating myocardium has been defined as a state of decreased contractility in response to chronic hypoperfusion in order to maintain tissue viability(Rahimtoola, *Circulation* 1982; 65:225–241). Previous experiments in our laboratory have investigated infarcted and stunned myocardium using Gd–DTPA with MRI(Pereira, *MRM* 2000; 44:309–316; Thornhill, *MRM* 2001; 45(5):864–871). In both cases, a constant infusion of Gd–DTPA was able to accurately differentiate damaged (either reversibly or irreversibly) from normal myocardial tissue. Gd–DTPA is excluded from normal and stunned myocytes, while allowed to distribute to infarcted myocytes, resulting in an increased partition coefficient (λ) and signal intensity on T1-weighted MR images in these infarcted regions. Since hibernating myocardium is still viable, our hypothesis is that the partition coefficient of Gd–DTPA and the signal intensity in these regions should be the same as normal tissue.

Purpose: In this preliminary study we critically stenose the left anterior descending (LAD) coronary artery to cause hibernation, not infarction, and test our hypothesis using MRI. Radioactive microspheres were used to confirm reduction in blood flow and radioactive measurements were also acquired to confirm tissue viability ex vivo.

Methods: The results from six canine experiments are reported in this study. Two sections of LAD were dissected free and a Transonic flow probe and occluding device were placed around these regions of the vessel. A balloon occluder was used for four experiments and plastic ties with rubber tubing were used for the other two. Microspheres were injected into the atrium to obtain baseline regional myocardial blood flow and during a transient occlusion to determine the region at risk (RAR). Flow was reduced to 30 ± 14% of baseline blood flow to create the stenosis. Microspheres were injected again 15 minutes after the stenosis. X-Ray angiography was performed on five dogs either following surgery or just prior to sacrifice to validate the patency of the stenosed vessel and confirm methodology. All imaging was performed on a whole-body 1.5 T MR system. Imaging was performed prior to surgery (n = 6), and 2 days (n = 6), 1 week (n = 4), 10 days (n = 4), 2 weeks (n = 5), and 3 weeks (n = 5) after surgery. At each imaging session Gd–DTPA was administered using a bolus followed by a constant infusion (Diesbourg, *MRM* 1992;23:239-253). Saturation recovery turboFLASH images were acquired pre- and post-contrast in order to quantify λ in vivo (2,5). Cine MR images were acquired for functional analysis. ^{201}Tl was injected 2.5 hrs prior to sacrifice and trace amounts of ^{111}In–DTPA were added to the Gd–DTPA infusion to measure tissue viability and ex vivo λ, respectively. Regional blood flow was measured again just prior to sacrifice, then the animals were sacrificed and the heart excised. The heart was sectioned into 60–155 pieces and each section counted for radioactivity to determine myocardial blood flow, viability and ex vivo λ.

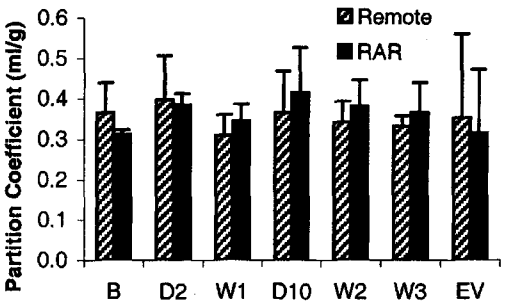

Figure 1. Ex vivo (EV) and in vivo partition coefficient results at baseline (B), 2 weeks (W1), 10 days (D10), 2 weeks (W2), and 3 weeks (W3). All are within range of normal tissue.

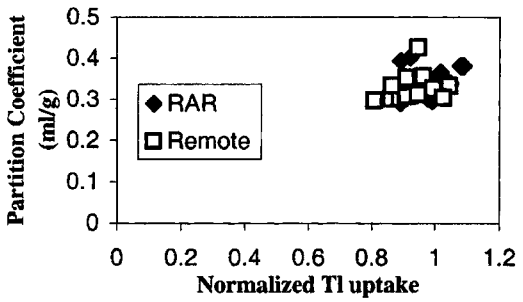

Figure 2. Tl uptake vs partition coefficient in 1 dog, indicating viable tissue in the RAR and remote tissue.

Results: Of the six dogs studied in this project, one animal showed a small region of infarct at 10 days after surgery but the large region of dysfunction could not be accounted for by the relatively small infarct zone and the study was carried out for the entire 3 week protocol.

Average in vivo partition coefficient results (± SD) are shown in Fig 1. Mean values ranged between 0.31–0.42 in the RAR tissue, and 0.31–0.40 in remote tissue, which are all within the range of normal tissue.

A representative graph of normalized Tl uptake vs Partition Coefficient is shown in Fig 2. Normalized Tl uptake and ex vivo λ are both within the range expected for normal myocardial tissue. The other five animals had similar results, indicating healthy tissue throughout the myocardium in all dogs.

Conclusion: Blood flow was reduced to the point of almost causing infarction while normal ^{201}Tl uptake was maintained and, thus, downregulation of function was necessary to maintain tissue viability. We conclude that a form of hibernating myocardium was created and the partition coefficient of Gd–DTPA was normal in this tissue. Therefore, reversibly damaged tissue, both stunned and hibernating, can be distinguished from permanently damaged tissue based on the partition coefficient of Gd–DTPA.

213. Quadruple Inversion-Recovery: A Method for Quantitative Contrast-Enhanced Black-Blood Imaging

Vasily Yarnykh,[1] Chun Yuan.[1] [1]*University of Washington, Dept. of Radiology, Box 357115, Seattle, WA, USA*

Introduction: Combination of black-blood (BB) T1-weighted imaging with contrast-enhancement (CE) offers a high potential for various cardiovascular applications, in particular, for high-resolution MRI of atherosclerotic plaque (1). However, due to significant shortening T1 in blood, traditional BB methods like double inversion-recovery (DIR) (2) or side-band saturation cannot guarantee an absence of flow artifacts on post-contrast images, which is especially important for quantitative analysis. In this study we propose a universal solution for CE BB imaging by introducing the principle of quadruple inversion-recovery (QIR) and compare this new method with traditional DIR technique.

Purpose: To develop the technique for quantitative BB CE imaging that would provide efficient flow suppression and tolerate variations in blood relaxation due to contrast administration.

Methods: Sequence. QIR is the preparative module consisting of two DIR blocks followed by inversion delays TI1 and TI2. Within each DIR block, a slice-selective adiabatic inversion pulse is applied immediately after a nonselective rectangular pulse. The blood magnetization is expected to approach zero after the time TI2 subsequent to the second double inversion. The QIR sequence was implemented on a 1.5 T MR scanner (GE Signa EchoSpeed) in combination with fast spin-echo (FSE) readout.

Theory. Longitudinal magnetization of blood outside an imaging slice in the presence of the QIR preparation is described by the equation:

$M_z=[1 - \exp(-TR/T_1) - 2\exp(-TI_2/T1) + 2\exp(-(TI_2 + TI_1)/T_1)]/[1 - \exp(-TR/T_1)]$ which has two zero solutions at predefined TR, TI1 and TI2 (Fig. 1).

MRI experiments. The effect of DIR and QIR preparations on the steady tissue signal was studied using a sample of fresh bovine muscle. To test the QIR sequence in vivo, the high-resolution T1-weighted images of carotid arteries were obtained from two carotid atherosclerosis patients (before and after contrast administration) and two healthy volunteers (without contrast injection). Informed consent was received from all participants. The protocol included DIR (TI = 325 ms) and QIR (TI1/TI2 = 375/125 ms) FSE scans with TR = 800 ms, TE = 11 ms, ETL = 8, 2 NEX, matrix 256 × 256, FOV 13 × 7 cm, slice thickness 2 mm. Post-contrast scans were acquired in 10–15 min after an injection of a gadolinium-based contrast agent ("Omniscan", 20 ml).

Results: Limitations of the DIR technique in CE applications. As was shown by simulations and phantom studies, the following limitations hamper an application of DIR for quantitative CE studies:

1. DIR provides efficient suppression of blood signal within a narrow range of T1 values at any chosen TI (Fig. 1). Thus, DIR is prone to flow artifacts caused by variations of T1 in blood after a contrast administration.

2. DIR is characterized by strong (up to 20% of relative change) dependence of a steady tissue signal on TI (Fig. 2). We have demonstrated that this dependence is determined mainly

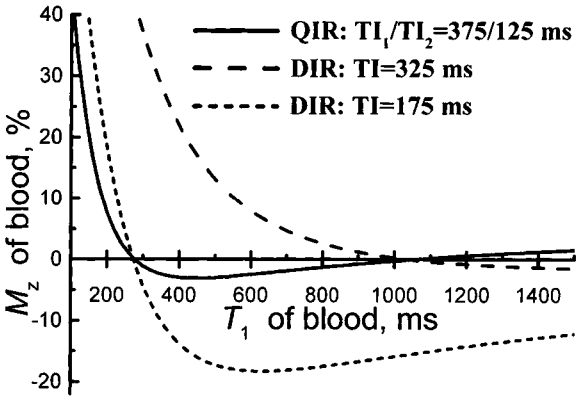

Figure 1. Simulations of inflowing blood magnetization for DIR and QIR sequences at TR = 800 ms.

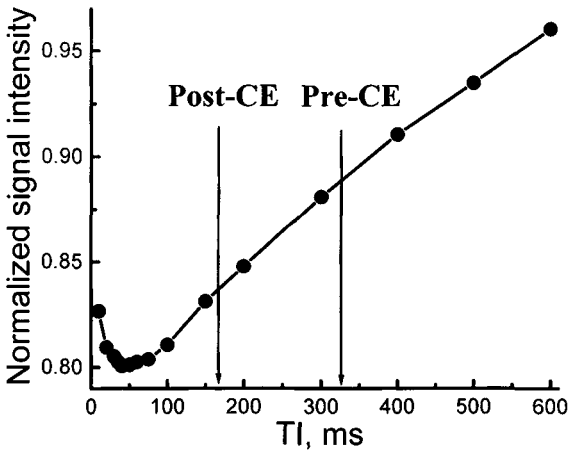

Figure 2. Effect of TI on tissue signal for DIR-FSE sequence (TR = 800 ms) measured using fresh bovine muscle. Arrows correspond to TI values required for pre- and post-contrast blood suppression.

by the magnetization transfer (MT) effect induced by the pair of inversion pulses. While the DIR sequence should be applied with different TI for pre- and post-contrast scans to obtain satisfactory blood suppression, it may cause a misinterpretation of the contrast enhancement in weakly enhancing tissues.

Features of the QIR sequence. The QIR preparation with properly chosen TI1 and TI2 provides efficient blood suppression in a wide range of T1 values (Fig. 1). In our protocol the parameters of the QIR-FSE sequence were adjusted to guarantee at least 90% blood suppression starting from expected T1 = 200 ms. It was sufficient for obtaining perfect lumen visualization in both arterial and venous vessels (Fig. 3). Note that unlike DIR, QIR does not require a precise knowledge of T1 for blood after a contrast injection, since the corresponding suppression curve is quite flat (Fig. 1). While QIR is subjected to a decrease of steady tissue signal due to MT saturation, similar to DIR, both pre- and post-contrast QIR images contain the same amount of MT effect, as they are obtained with the identical pulse sequence. It allows one to attribute quantitative changes of signal intensity to the influence of a contrast agent only. Although the saturation of steady tissues by the QIR sequence appeared to be slightly higher than that for DIR preparation (3–9% of additional signal decrease), this effect was too small to affect the overall image quality.

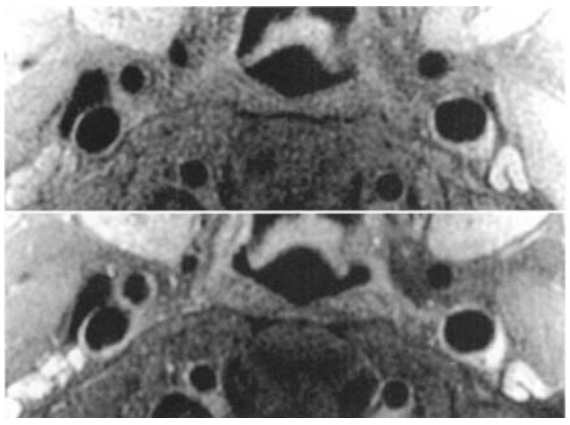

Figure 3. Pre- (top) and post-contrast (bottom) T1-weighted QIR-FSE images of a carotid atherosclerosis patient.

Conclusion: QIR preparation allows high-quality T1-weighted black-blood images to be obtained both before and after administration of the gadolinium-based contrast agent. The proposed method provides reliable quantitative interpretation of a contrast enhancement in tissues and can be recommended for a wide spectrum of cardiovascular applications.

References

1. Yuan C, Ferguson M, Kerwin W et al. *Proc. ISMRM* 2001; p.641.

2. Edelman RR, Chien D, Kim D. *Radiology* 1991;181:655–660.

214. A Total Non Invasive Assessment of Cardiac Function

Benjamin Cocheteux,[1] Serge Willoteaux.[2] [1]*Lille 2 University, Blvd du Pr Leclercq, Lille, Nord (59), France;* [2]*Lille university hospital, vascular radiology, bvd Pr Leclercq, Lille, Nord (59), France*

Introduction: Cardiac MRI allows heart functionals parameters to have an access with non invasive method, such as volumes, flows or velocity. We chose to study a complex specific left myocard contractility parameter, the telesystolic elastance (Tse), which is a hemodynamic research parameter, not accessible in clinical practice because of its invasive measurement.

Purpose: To show it is possible to quantify a functional left ventricular specific parameter, the telesystolic elastance (Tse), with an MRI non invasive method, fiting a physiologic model, giving us cardiac energetic metabolism information, and to demonstrate a simple technic realisation to use a such physiologic parameter in clinical MRI.

Methods: The studied group is composed of 39 subjects. It was composed of 25 voluntary healthy subjects (18 men and 7 women; middle age, 28.3; standart deviation, 10.1 range, 19–73), without cardiac failure, and with normal arterial pressure. The 14 other subjects already underwent a cardiac MRI within the framework of a Right Ventricular Arythmogenic Dysplasia (RVAD) suspicion and whose diagnosis was no carried (7 men and 7 women; middle age, 39.6; standart deviation 9.7; range, 21–57). The data acquisition consisted of recording the brachial arterial pressure and secondly, the telesystolic volumes computed by semi automated software segmentation. We propose it a single beat measurement, in a left ventricular healthy subject population Tse got such as Tse = Middle arterial pressure/Telesystolic volume. In order to improve the result's validity and truth, we did an intra observator varaiability study, to get an autovalidation of the data.

Results: Our average value of Tse was near of average value in catheterrism publication: respectively 2.33 ± mmHg

ml − 1, range 1.26 to 3.88 for us, against 2.24 ± 0.61 mmHg ml − 1. The middle arterial pressure wa to [92.1 ± 7.17, range 80 to 104.6] mmHg. The telesystolic volume measured was to [43.72 ± 13.3, range 27.9 to 79.02] ml, autovalidated by a velocimetric ejection volume measure method, and the indexed left myocardial mass calculated was to [79.02 ± 27.09, range 48.23 to 106.9] g m − 2. The intra observator study showed a variabilty of 4.06 ± 3.94%, for the systolic ejection volume, 5.22 + -5% for the left ventricular mass, and 4.39 ± 3.94% for the left ventricular telesystolic volume. The inter observator study show a results variability about the systolic ejection left ventricular volume of 4.08%, 3.22% about the left ventricular mass, and 6% about the telesystolic volume.

Conclusion: The non invasive measure of the left ventricular telesystolic elastance is a ventricular parameter available by MRI, which allows a functional approach of the left ventricular remodeling, in addition of other functionals cardiac, aortic and vascular functionals parameters, the cardiac mass, the morphologic myocardial remodeling study, and the contraction aspect, semi quantitatives parameters, in order to apply it in high prevalence cardiac deseases such as heart failure or hypertension.

Figure 1. In vivo long-axis image of Radius nitinol coronary stent using the multi-slice sequence (0.4-mm resolution $\alpha = 90°$).

215. MRI of Nitinol Coronary Stents: Implications for Assessing Stent Patency and Guiding Interventions

Masahiro Terashima,[1] Phillip C. Yang,[1] Bob S. Hu,[1] Erasmo De La Pena-Almageur,[1] Craig H. Meyer,[1] Krishna S. Nayak,[1] John M. Pauly,[1] Dwight G. Nishimura,[1] Michael V. Mcconnell.[1] [1]*Stanford University, Cardiovascular Medicine and Electrical Engineering, Stanford, California, United States*

Introduction: Coronary stenting has become the primary catheter-based therapy for coronary stenoses due to lower rates of restenosis. However, the image artifacts of conventional stainless steel stents threaten to limit the current and future utility of coronary MRA in the noninvasive evaluation of coronary artery disease. In addition, the development of interventional MRI requires stents that can be imaged during and after deployment to determine procedural success. Coronary stents made of nitinol generate less artifact and may allow assessment of stent patency, in-stent restenosis, and real-time imaging of deployment success.

Purpose: Evaluate coronary and real-time MRA imaging within nitinol coronary stents.

Methods: A total of 5 coronary stents were imaged *in vivo* in the aorta of 3 rabbits (nitinol: 4.0 × 18 mm (N = 2); stainless steel: 4.0 × 13 mm) and *ex vivo* in saline (nitinol: 3.0 × 20 mm; stainless steel: 4.0 × 18 mm). Stents were placed in the rabbits under x-ray fluoroscopic guidance and MRI was performed 2 and 14 days after stent implantation. A 1.5 Tesla GE Signa scanner was used, equipped with high-performance gradients (40 mT/m, 150 mT/m/ms) and a real-time interactive workstation. We performed long- and short-axis imaging using a multi-slice (MS) coronary sequence (0.6-mm resolution, TR—1 sec, 20-cm FOV, 5 mm thickness) and a real-time (RT) coronary/interventional sequence (1.1-mm resolution, 20-cm FOV, 12-30 fps). Flip angle was varied from 30° to 90°. A high-resolution version of the MS sequence was also performed (0.4-mm resolution, 16-cm FOV, 3-mm thickness, NEX = 2), as well as a RT color-flow MRI sequence to image flow within the stent (2.4-mm resolution, 20-cm FOV, 18 fps). In-stent diameter, length, and SNR were measured.

Results: Both ex vivo and in vivo, MRI successfully imaged inside the nitinol, but not stainless steel, coronary stents, using both MS and RT sequences (Figure 1 and 2). In addition, RT color-flow MRI demonstrated good flow signal within the in vivo nitinol stents. On both MS and RT images, SNR inside the stent improved with increasing the flip angle to 90°, both qualitatively and quantitatively (21% increase from 60° to 90°). In-stent diameter of nitinol coronary stents was 29% smaller

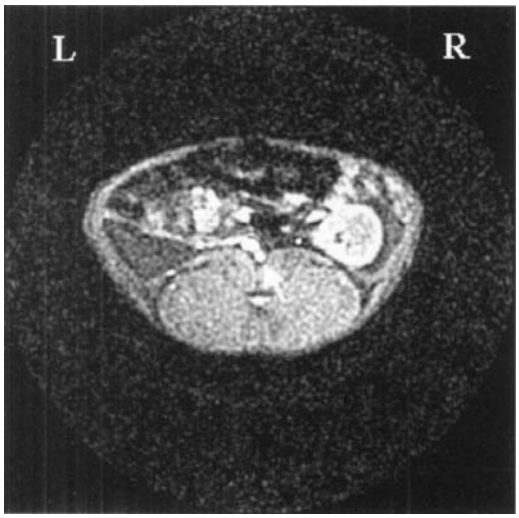

Figure 2. In vivo short-axis image of Radius nitinol coronary stent using the real-time sequence (1.1-mm resolution, $\alpha = 90°$).

and length was 15% larger than measured on x-ray angiography.

Conclusion: MRI can perform angiographic and flow imaging inside coronary stents made of nitinol, using both coronary MRA and real-time sequences. Translation to human studies may allow noninvasive assessment of stent patency/restenosis as well as real-time interventional MRI guidance of stent deployment.

216. Angiotensin II Type 2 Receptor Overexpression Improves Regional Function After Myocardial Infarction

Christina M. Bove,[1] Frederick H. Epstein,[1] Joseph M. Dimaria,[1] Wesley D. Gilson,[1] Zequan Yang,[1] Brent A. French,[1] Stuart S. Berr,[1] Christopher M. Kramer.[1] [1]*University of Virginia, Cardiovascular Div. and Depts. of Radiology and Biomedical Engineering, Charlottesville, Virginia, United States*

Introduction: Early after myocardial infarction (MI), regions adjacent to the infarct demonstrate contractile dysfunction that persists and is associated with left ventricular remodeling[1]. Recently, MRI tagging has been applied to the study of regional differences in contractile function after MI in mice[2]. The angiotensin II type 2 receptor (AT_2-R) may mediate much of the beneficial effects of renin–angiotensin system blockade post-MI. Preliminary MRI data from our group demonstrates that cardiac AT_2-R overexpression in the mouse preserves global left ventricular function from day 1 to 4 weeks post-MI[3].

Purpose: We hypothesized that MRI tagging would localize improvements in regional myocardial function early after MI in AT_2-R overexpressed mice.

Methods: Animal Model

Four male wild-type (WT) C57BL/6 mice and 6 transgenic (TG) mice which overexpress the AT_2-R in the heart were studied by cardiac MRI prior to infarction (day 0) and 24 hr. post-MI (day 1). MI was induced by a 1 hour occlusion of the LAD followed by reperfusion. Infarct size in this model is quite reproducible with a mean size of 34 ± 5% of total LV mass at day 1 post-MI.

Mouse Imaging

Anesthesia was induced with 3.0% inhaled isofluorane and mantained with 1.0% isofluorane. Cine and tagging MRI was performed on a Varian Inova (Varian, Inc., Palo Alto, CA) 4.7 T scanner. Twenty minutes prior to imaging on day 1 post-MI, 0.3 mM/kg gadolinium–DTPA (Gd) was infused intraperitoneally to assess infarct size. An ECG-triggered 2D cine FLASH sequence was used to obtain 7–8 1 mm thick short axis slices from apex to base (Figure 1C). Cine imaging used TE = 3.9 ms and TR was adjusted (8.0–14.0 ms) to obtain 16 phases per cardiac cycle. A 60° flip angle was used to increase the amount of T1 weighting in post-Gd imaging. A 2.56 cm × 2.56 cm FOV was used with a matrix of 128 × 128. The tagging sequence used a 6-lobe SPAMM RF pulse applied immediately after the ECG trigger and multi-slice FLASH acquisition. The FLASH acquisition used TR = 2 heart beats, TE = 5.5 ms, FOV = 2.56 cm, matrix size = 192(readout) × 96 (phase encode), slice thickness = 1 mm (no inter-slice gap), and flip angle = 30°. Additionally, the tag pulse flip angle was 180° and the tag separation was 0.7 mm. Six signal averages were used to reduce respiratory motion artifact and increase the signal-to-noise ratio. Six slices each with 6 cardiac phases covering systole were acquired per orthogonal 1D tag direction.

Data Analysis

The infarct region was defined as the area of delayed hyperenhancement in day 1 post-Gd images where the signal intensity was greater than 2 standard deviations above the mean of remote regions. Percent circumferential shortening (%CS) was measured from tagged images using the Findtags program and 12 sectors per slice. Epicardial and endocardial borders used for tag analysis were traced from the corresponding cine FLASH images. A 12 sector model was aligned such that 2 sector borders matched the Gd-enhanced borders. Sectors within the Gd-enhanced region were termed infarct (inf), those bordering either side of the infarct in the short axis were termed adjacent (adj), and all remaining sectors remote (rem). On day 1 images, all slices containing approximately 40–60% of the myocardial area with transmural contrast enhancement were subject to strain analyis (Figure 1D). For day 0 images, 2–3 corresponding slices were chosen for strain analysis. Mean %CS was calculated at day 0 and at day 1 for each zone in WT and TG mice. Two-way ANOVA confirmed intragroup differences by region and time point ($p < 0.001$). Regional and between group differences in %CS were analyzed using pairwise multiple comparisons subtesting (Tukey test).

Results: Infarct size was similar between groups. Mean %CS at day 0 and regional %CS at day 1 are shown in Table 1 on next page. Baseline %CS was similar for WT and TG mice. At day 1 post-MI, mild remote region dysfunction was noted in both groups. Within the infarct region, stretching was noted in WT mice (%CS -2.2 ± 0.6%), whereas shortening was found in TG mice (2.5 ± 0.5%, $p < 0.001$). Adjacent region dysfunction was present in both groups, but %CS was significantly higher in the

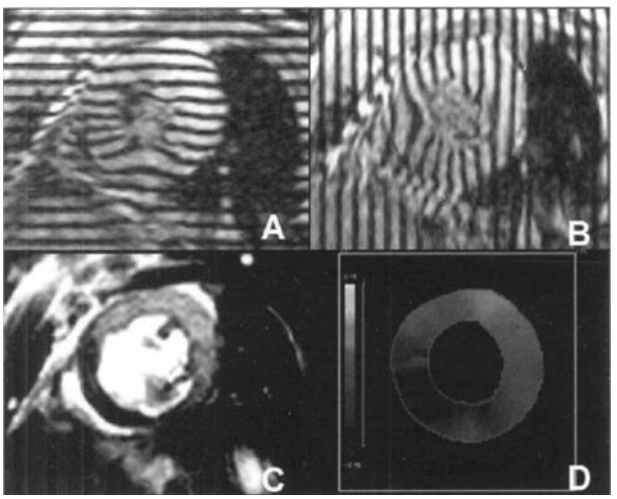

Figure 1. End-systolic tagged images (A,B), end-diastolic Gd-enhanced cine image (C) and %CS map (D) of a TG mouse day 1 post-MI. The hyperenhanced infarct is seen from 10 to 4 o'clock (C) and demonstrates reduced deformation (A,B) (red color on D).

Table 1

%CS at Day 0 and at Day 1 in Rem, Adj, and Inf Zones

	Day 0	Day 1 Rem	Day 1 Adj	Day 1 Inf
WT	15.5 ± 0.5	13.4 ± 0.7*	6.2 ± 1.0*†	−2.2 ± 0.6*†‡
TG	15.6 ± 0.3	12.5 ± 0.5*	9.4 ± 0.8*†	2.5 ± 0.5*†‡
p value	NS	NS	<0.02	<0.001

*$p < 0.001$ vs Day 0; †$p < 0.001$ vs. rem; ‡$p < 0.001$ vs. adj.

adjacent region in TG mice (9.4 ± 0.8%) compared to WT (6.2 ± 1.0%, $p < 0.02$).

Conclusion: MRI tagging can detect regional differences in contractile function post-MI in transgenic mice. AT_2-R overexpression in the murine heart is associated with improved contractile function within infarcted and adjacent noninfarcted regions on day 1 post-MI. Further studies will determine if the improvements in regional function persist at later time points post-MI and determine the mechanisms underlying the beneficial effects of AT_2-R overexpression.

217. MRI Shows Contrast Enhancement in Rabbit Atheromas

Ralf Wassmuth,[1] Jonathan Sorger,[2] Bruce Wasserman,[3] Joni Taylor,[2] Andrew Arai.[2] [1]*Humboldt University Berlin, Wiltbergstr. 50, Berlin, Germany;* [2]*National Institutes of Health, 10 Center Drive, Bethesda, Maryland, USA;* [3]*Johns Hopkins University, JH Medical Institutions E Balt, Baltimore, Maryland, USA*

Introduction: Magnetic resonance imaging (MRI) can visualize atherosclerotic plaques in animal models.In how far atheromas enhance after contrast administration is unclear.

Purpose: We tested in a rabbit model of premature atherosclerosis whether Gadolinium administration adds any benefit.

Methods: We studied 17 LDL-receptor-deficient rabbits (3.4 ± 0.4 kg) and 17 New Zealand controls (3.3 ± 0.5 kg) in a 1.5 T MRI scanner using an extremity coil. T1-weighted spin echo images (TR 545 ms, TE 7.4 ms) of the thoracic and abdominal aorta were obtained in vivo before and after 0.1 mmol/kg BW Gd–DTPA was administered. Spatial resolution was 0.39 mm/pixel within a 3 mm slice. The plaque signal was compared to vessel walls in controls and adjacent muscle in diseased animals with Student's *t*-test.

Results: Plaques could be identified in all diseased animals and were confirmed by ex vivo HE staining of corresponding slice locations. The average lesion tickness was 0.89 ± 0.27 mm. In controls thin aortic walls were barely visible. Contrast data were available in 14 diseased animals and 12 controls. After contrast the lesion signal increased (+37.3 ± 13.2%). Intimal thickening, non-calcified and calcified lesions were found in histology. Most plaques showed a homogeneous enhancement independent of histologic stage. Some atheroma clearly showed a mixture of fibrous and lipid rich components on review of histology but demonstrated uniform contrast enhancement on MRI. Both, adjacent skeletal muscle in diseased animals and vessel walls in controls showed only minimal enhancement (5.1 ± 4.6%, and 12 ± 19%, $p < 0.0002$ for both).

Conclusion: Contrast administration increases the MRI signal of atherosclerotic plaques in rabbits but does not allow differentiation of plaque components.

218. Vascular Injury Induces Immediate and Delayed Contrast Enhancement, Remodeling, and Atherosclerosis

Masahiro Terashima,[1] Phillip Yang,[1] Erasmo De La Pena-Almageur,[1] Bob Hu,[1] Michael Mcconnell.[1] [1]*Stanford University, Cardiovascular Medicine, Stanford, California, United States*

Introduction: Vascular injury can cause an inflammatory response that contributes to atherosclerotic plaque formation and restenosis. Conventional imaging techniques do not directly image the vessel wall. Contrast-enhanced MRI (CEMRI) may improve characterization of the vessel wall, particularly biological changes such as inflammation.

Purpose: We tested the feasibility of CEMRI to monitor the response to vascular injury noninvasively.

Methods: Six New Zealand White rabbits were fed a hyperlipidemic diet for 1 week, then underwent focal balloon injury (3F Fogarty) of the abdominal aorta. On a 1.5 T system,

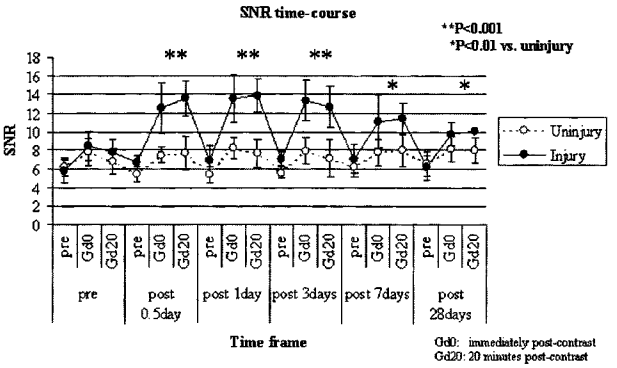

Figure 1. SNR time-course of both the injured and uninjured vessel wall.

T1-weighted fast spin echo MRI was performed pre- and immediately post-contrast (0.1 mmol/kg Gd–DTPA, 16 cm FOV, 0.3 mm resolution, 370 ms TR, 34 ms TE). MRI was repeated 20 minutes after contrast injection to estimate prolonged enhancement in the vessel wall. The imaging protocol was repeated up to 28 days after balloon injury when animals were sacrificed. Signal-to-noise ratio (SNR) of the injured and uninjured aortic segments at each time point was measured on 584 images in order to assess contrast enhancement. Comparison of CEMRI between injured and uninjured segments was performed using a two-way factorial ANOVA.

Results: CEMRI demonstrated both immediate and delayed enhancement of the injured vessel wall segments (Figure). Enhancement was significantly greater in the injured vs. uninjured segments ($p < 0.001$). While the degree of enhancement appeared to decrease over 7 to 28 days post-injury, the effect remained statistically significant. Vessel wall area was found to have increased by 45% at injured segments vs. 13% at uninjured segments. Histology at 28 days after balloon injury showed focal atherosclerosis and intramural hematoma at injured segments, with only mild intimal thickening at uninjured segments.

Conclusion: CEMRI can visualize vascular changes after balloon injury and may improve MRI characterization of the vessel wall.

219. The Effect of Diabetes on the Constant-Volume Attribute of the Four-Chambered Heart

Andrew Bowman,[1] Shelton Caruthers,[1] Mary Watkins,[1] Sándor Kovács.[1] [1]*Washington University in St. Louis, 660 S. Euclid Ave, St Louis, Missouri, United States*

Introduction: Previous studies in dogs using the dynamic spatial reconsructor have shown that the total volume of the pericardial sack remains constant (within a few percent) throughout the cardiac cycle. Others have reported that pericardial volume in humans remains constant for parts of the cardiac cycle. However, no study has demonstrated constancy of human pericardial volume throughout the cardiac cycle using current magnetic resonance imaging (MRI) technology. The pathophysiologic consequences of insulin dependent diabetes mellitus (IDDM) are known to include development of microvascular disease resulting in tissue remodeling and altered chamber properties. Myocardial–pericardial interaction as a consequence of IDDM has not been previously characterized.

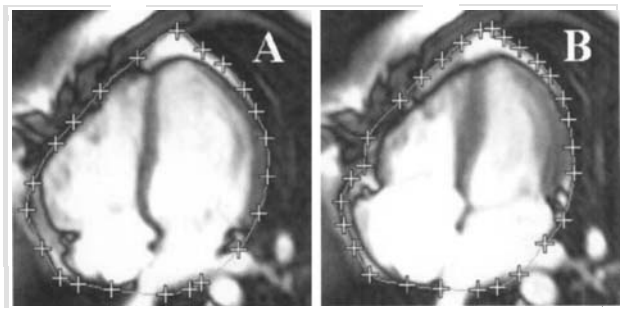

Figure 1.

Purpose: The conventional approach to characterizing the pathophysiologic sequelae of diabetes at the organ (whole heart) level include determination of invasive and noninvasive measures of systolic and diastolic function, chamber properties, and propensity for development of ischemia. The principal noninvasive indexes characterize ejection fraction, peak filling and ejection rates, isovolumic contraction and relaxation intervals, and deceleration time of the transmitral Doppler E-wave. Prior noninvasive or invasive methods have been unable to determine the location and motion of the pericardial contour as a measure of summed atrial and ventricular volumes to adequate precision and are not suited for determining if there is a pericardial–myocardial interaction different from normal in the setting of IDDM. Cardiac MRI is the gold standard for noninvasive determination of chamber volume and shape, LV mass and motion, and pericardial location and motion.

Methods: Six normal (NL) volunteers and six subjects with IDDM underwent MRI studies on a 1.5 T Philips Gyroscan. The two-dimensional analogue of the four-chamber heart volume was quantitated as the area of the manually traced pericardial contour (Apc) for each phase of the four-chamber cine-loop using Philips EasyVision software. To provide an estimate of for the percent variation of four-chambered volume, the smallest Apc measured during the cardiac cycle was subtracted and divided by the Apc at end-diastole.

Results: For the NL group, Apc-NL varied $4 \pm 2\%$ from the end-diastolic Apc. For the IDDM group, Apc-IDDM varied $6 \pm 2\%$ ($p < 0.05$). In both groups, the maximum variation occurred at end-systole. No clear anatomical region appeared to account for the increased variation in the Apc of the IDDM group. The figure shows the contour of the same NL subject at end-diastole (A) and end-systole (B).

Conclusion: Cardiac MRI demonstrates that two-dimensional pericardial content in non-diabetic human controls varies by 4% throughout the cardiac cycle. In IDDM, the pericardial content is more variable. We conclude that the constant-volume attribute of the four-chambered heart can be accurately estimated using current MRI techniques and may be altered in IDDM. Increased variation of this two-dimensional measure is consistent with a myocardial–pericardial interaction in diabetes that differs from normal. To exclude two-dimensional shape change effects as the explanation, determination of four-chamber pericardial volume in subjects with IDDM using three-dimensional data sets is in progress.

220. End-Systolic Versus End-Diastolic Displacement of the Mid-Papillary Muscles: A Novel Index of Ventricular Twist and Translation

Andrew Bowman,[1] Shelton Caruthers,[1] Mary Watkins,[1] Sándor Kovács.[1] [1]*Washington University in St. Louis, 660 S. Euclid Ave, St Louis, Missouri, United States*

Introduction: As a consequence of the helical fiber structure of the LV wall, left ventricular (LV) systolic ejection generates twisting of the LV apex relative to the LV base. In normal,

healthy individuals at rest, the maximum twist of the apex relative to the base has been observed on average to be about 12–14 degrees, while the maximum twist at the mid-papillary muscle level has averaged 5–6 degrees. The majority of systolic twist occurs during isovolumic contraction, and the majority of myocardial untwisting in diastole occurs during isovolumic relaxation. The papillary muscles (PM) and chordae act as a systolic force member connecting the mitral annulus (via the coapted leaflets) to the apicolateral endocardial surface where the papillary muscles insert. Characterization of the motion of the PMs relative to LV twist has not been previously performed. Cardiac magnetic resonance imaging (MRI) is the gold standard for quantitating the amount of LV twist via myocardial tagging and provides optimal views of PM location and motion in short-axis views.

Purpose: We hypothesize that LV end-systolic versus end-diastolic twist and translation can be quantitated using non-tagged short-axis, mid-papillary images. Due to their unique anatomical location within the LV, the PMs must also twist and translate during the cardiac cycle. We sought to show that in normal subjects, the displacement of the centers of the PMs (as seen in a short-axis image) relative to each other (measured as rotation of a line that connects the centers of the PMs) is concordant with the net twist experienced by the LV as a whole and conveys information regarding translational motion as well.

Methods: Five normal subjects underwent cardiac MRI studies on a 1.5 T Philips Gyroscan. Short-axis cine loops covering most of the cardiac cycle were obtained at the mid-papillary muscle level in each subject. Raw images were converted to JPEG files, exported to a remote console, and analyzed using Paint Shop Pro 5. Images at end-diastole and end-systole were selected. The coordinates of the middle of the PMs were obtained in each image and connected to generate the mid-papillary line (MPL) in each image. The estimated MPL twist is given by the measurement of the angle of rotation between the mid-papillary line at end-diastole versus end-systole. MPL translation is given by the distance (normalized to the end-diastolic MPL length) a given papillary muscle shifts between end-diastole and end-systole.

Results: The mid-papillary line rotated within the image plane by an average of 5.1 ± 3.3 degrees. The average PM translation was 19 ± 5% of the end-diastolic MPL length. The axis of rotation was intra-chamber in 3 of 5 subjects. In 2 of 5 cases, location of the MPL axis of rotation was external to the LV chamber. The figure shows the superposition of the MPL at end-diastole (red line) and at end-systole (green line) in images of both end-diastole (A) and end-systole (B) for one subject.

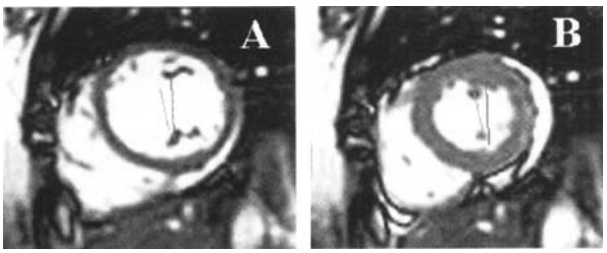

Figure 1.

Conclusion: In concordance with the twist of the LV as a whole, the PMs define MPL twist in the same direction as the LV wall. The axis of twist was located within the LV chamber in 3 of 5 subjects. The location of the axis of MPL twist external to the LV chamber indicates that translation was greater than the product of twist (in radians) and MPL length. These measurements provide novel insight into the role of the papillary muscles as force transduction members that couple the mitral valve plane to the LV wall during systole. The measurements of PM translation and twist may be used to estimate LV torsion throughout the cardiac cycle in both normal and diseased states. Validation of this technique and the significance of intra- versus extra-chamber location of the axis of rotation using myocardial tagging and application to diseased states are in progress.

221. Myocardial Infarction Alters the MRI-Determined Ventricular to Atrial Blood Volume Ratio at Diastasis

Andrew Bowman,[1] Shelton Caruthers,[1] Mary Watkins,[1] Sándor Kovács.[1] [1]*Washington University in St. Louis, 660 S. Euclid Ave, St Louis, Missouri United States*

Introduction: Numerous alternative definitions of left ventricular equilibrium volume (LVEV) have been proposed. One definition for LVEV uses the volume of the LV when the transmural pressure gradient, referred to atmospheric pressure, is zero. Because accurate transmural pressure gradient determination in-vivo cannot be achieved, we have previously reasoned that the LVEV is the volume at diastasis. The LVEV is attained when the atrioventricular pressure gradient is zero, transmitral flow is absent, and all forces are balanced; hence, the transmural pressure gradient is immaterial. This definition uses the pressure of the source chamber for filling (left atrium) relative to which LV pressure equilibrates, rather than the atmospheric pressure. Furthermore, this definition for LVEV required that all ventricles that generate an early, rapid-filling phase (Doppler E-wave) must have LV end-systolic volume <LVEV (diastatic volume) and must be mechanical suction pumps because $dP/dV < 0$ at mitral valve opening.

Purpose: We hypothesize that the ratio of the volume of blood in the ventricles to that in the atria at diastasis defines a state of equilibrium and therefore comprises a novel

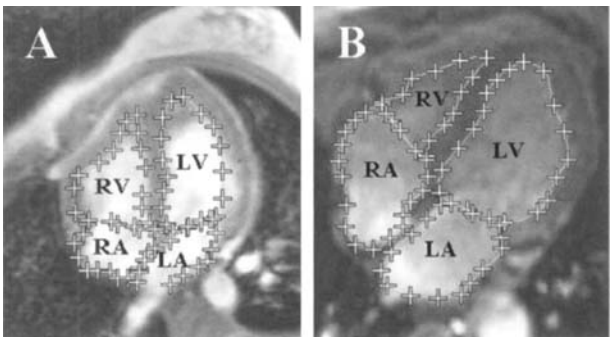

Figure 1.

dimensionless index that may be altered in diseased states. The two-dimensional (2-D) analogues of these volumes can be obtained as the respective areas of the four-chamber slice via magnetic resonance imaging (MRI), the gold standard for in-vivo, noninvasive heart chamber volume determination.

Methods: Six normal volunteers and six patients with a history of myocardial infarction (MI) had MRI exams using a 1.5 T Philips Gyroscan. Diastasis images from four-chamber cine loops were selected. 2-D areas of the left and right atria and ventricles were planimetered using Philips EasyVision software.

Results: In the normal group (figure 1A), the ratio of (left + right ventricular area) to (left + right atrial area) [(LV + RV)/(LA + RA)] = 2.3 ± 0.3, while in the MI group (figure 1B), the ratio is 1.5 ± 0.3 ($p < 0.001$).

Conclusion: Myocardial infarction lowers the combined ventricular blood volume (VV) to atrial blood volume (AV) ratio at diastasis in the four-chambered heart. The lowering of this ratio after MI reflects alteration of LVEV either by an increase in increase in atrial volume (relative to control) or a decrease in LV blood volume (relative to control). Since MI is known to increase chamber size, alter chamber properties (i.e. increase stiffness), and result in remodeling, the probable explanation for lowering VV/AV is that atrial volume is increased post MI. Decrease of the VV/AV ratio may contribute to impairment of systolic and diastolic function post MI, alteration of chamber properties (increased stiffness) associated with remodeling, and may contribute to the decreased systolic and diastolic function post MI. Further validation of this new, MRI-based index of four-chambered heart function is in progress.

222. MR Assessment of Myocardial Oxygen Extraction Fraction: Theoretical Consideration

Jie Zheng,[1] Dmitriy Yablonskiy,[2] Mark Nolte,[1] Debiao Li,[3] Nikolaos Tsekos,[4] Robert Gropler.[2] [1]*Washington University in St. Louis, Mallinkcrodt Institute of Radiology, St. Louis, Missouri, United States;* [2]*Washington University in St. Louis, Medical School, Saint Louis, Missouri, United States;* [3]*Northwestern University, Department of Radiology, Chicago, Illinois, United States;* [4]*Mallinckrodt Institute of Radiology, Cardiovascular Imaging Lab, St. Louis, Missouri, United States*

Introduction: Myocardial oxygen extraction fraction (OEF) represents the relationship between myocardial oxygen supply and demand. Due to the heterogeneity of myocardial blood flow distribution, that particularly occurs in coronary artery disease, it is important to assess the regional difference of myocardial OEF. However, to date myocardial OEF has not been successfully quantified yet. In this project, it is hypothesized that the measurement of myocardial transverse relaxation time (T2) will lead to a quantification of regional myocardial OEF.

Purpose: The aim of this study is to develop a theoretical MR model for quantifying myocardial T2 and regional OEF based on the blood oxygenation level-dependent (BOLD) effect. An Initial in vivo assessment on the model was performed in dogs.

Methods: **Theoretical Model:** The myocardial BOLD signal change could be described with a two-compartment

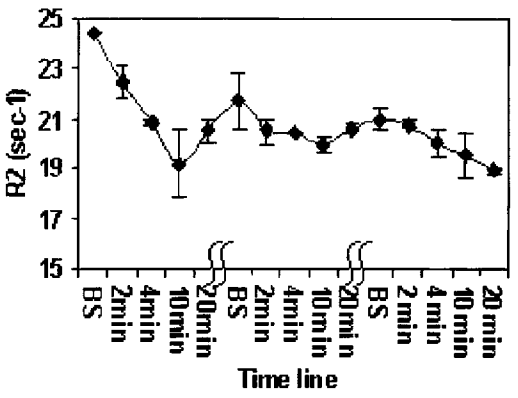

Figure 1.

model: intracapillary (<10%) and extravascular compartments (>90%). The $R2_{voxel}$ ($1/T2_{voxel}$) in a voxel containing capillaries and myocardial tissue can be given by:

$$R2_{voxel} = MBV*R2_{capillary} + (1 - MBV)*R2_{tissue} \quad (1)$$

in which $R2_{tissue}$ and $R2_{capillary}$ are the reciprocals of T2 of the myocardial tissue and capillary blood, respectively. The MBV is the myocardial blood volume fraction. Based on the model developed by van Zijl et al. [1] in the brain functional imaging, the R2capillary in the capillary as a function of oxygen extraction fraction (OEF) is given as:

$$R2_{capillary} = 2.36*OEF2 + 3.77*OEF + 1.92\,(sec^{-1}) \quad (2)$$

$$R2_{tissue} = R2_0 + R2_{diff} \quad (3)$$

where $R2_{diff}$ is the T2 relaxivity due to the signal loss in the extravascular space caused by spin diffusion in the presence of field inhomogeneity created by paramagnetic effect of deoxyhemoglobin. $R2_0$ is an intrinsic myocardial tissue R2. Assuming a parallel capillary system in the myocardium [2], the $R2_{diff}$ can be estimated as: $R2_{diff} = A*OEF^2$. The parameter A is a function of MBV and Hct and is estimated as 4.0 sec_{-1}, assuming hematocrit 0.4 and MBV 0.06 (previous experimental

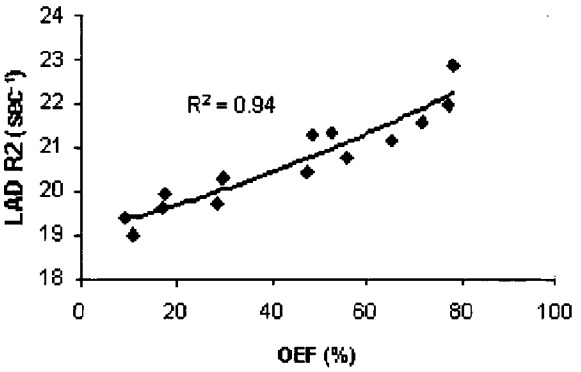

Figure 2.

data). We will determine $R2_0$ and A from curve fitting using experimental data based on Eqs. (1), (2), and (3).

In vivo Exam: Two dogs were scanned with a segmented double-echo 2D turbo spin echo sequence with TE1 = 5.3 ms and TE2 = 74 ms. Three doses of dipyridamole, i.e., 0.05, 0.1, and 0.15 mg/kg/min, were infused consecutively at a time interval of 60 min. Myocardial T2 was measured on a short-axis plane at baseline (BS), 2 min, 4 min, 10 min, and 20 min at each dose. In one dog, blood samples were collected at those times from both descending thoracic aorta and coronary sinus to measure myocardial OEF invasively.

Results: Figure 1 demonstrates the change of myocardial R2 in the ventricular septa at different times of vasodilation. The myocardial R2 decreases after the infusion of dipyridamole due to decreased deoxyhemoglobin content secondary to the increased blood flow and then recoveries after approximately 10–15 min. Fig. 2 shows the R2 changes in the myocardium of LAD territory as a function of measured OEF. The curve fitting of these data results in the $R2_0 = 20.6\,sec^{-1}$ and $A = 4.5\,sec^{-1}$, which is in excellent agreement with the theoretical predicted value.

Conclusion: Using deoxyhemoglobin as a natural intravascular contrast agent, our work demonstrates the possibility to evaluate myocardial OEF from measurements of myocardial T2 and BOLD effect. This quantification will provide fundamental information on myocardial oxygenation and when combined with measurements of myocardial blood flow permit measurement of myocardial oxygen consumption. In addition, when combined with vasodilator stress the method may provide a putative measurement of myocardial flow reserve and/or allow consecutively monitoring dose-responses of myocardium to various interventions.

References

1. van Zijl PC, et al. Nat Med 1998; 4:159–167.
2. Bauer WR, et al. Magn Reson Med 1999; 41:51–62.